

# Angular Light Scattering of Gold Nanoparticles on Graphene Oxide

Master's thesis in Master Programme Applied Physics

HÜSEYİN TEPE



MASTER'S THESIS 2016:NN

# Angular Light Scattering of Gold Nanoparticles on Graphene Oxide

HÜSEYİN TEPE



**CHALMERS**  
UNIVERSITY OF TECHNOLOGY

Department of Physics  
*Division of Chemical Physics*  
CHALMERS UNIVERSITY OF TECHNOLOGY  
Gothenburg, Sweden 2016

Angular Light Scattering of Gold Nanoparticles on Graphene Oxide  
HÜSEYİN TEPE

© HÜSEYİN TEPE, 2016.

Examiner & Supervisor: Prof. Dinko Chakarov, Chemical Physics, Department of Physics

Master's Thesis 2016:NN  
Department of Physics  
Division of Chemical Physics  
Chalmers University of Technology  
SE-412 96 Gothenburg  
Telephone +46 31 772 1000

Cover: Illustration of a gold nanoparticle on graphene oxide, which scatters the incident light to different directions with different wavelengths.

Typeset in L<sup>A</sup>T<sub>E</sub>X  
Printed by Reproservice  
Gothenburg, Sweden 2016

Angular Light Scattering of Gold Nanoparticles on Graphene Oxide  
HÜSEYİN TEPE  
Department of Physics  
Chalmers University of Technology

## Abstract

Lately, the study of plasmon excitations have been a rapidly growing subject. Some applications are light trapping, sensing and catalysis. The scattering characteristics of particles depends on the size of the particle and the environment. The aim of this study is to perform angular resolved measurements on gold nanoparticles imbedded in graphene oxide flakes. The angular scattering intensities and peaks were measured. The effect of changing environment on the scattering spectrum was also studied. Peak shifts were observed for changing dielectric environment.

Changing the dielectric environment, from a citric buffer to graphene oxide on fused silica, led to a peak shift from  $541\text{ nm}$  to  $573\text{ nm}$ . The angular intensity measurements revealed possibly a diffraction pattern, which changed for different wavelenghts. Angular scattering measurements showed the weakness of the sample preparation method. The sample was therefore modified, and angular scattering measurements were conducted, which showed different scattering peaks at different observation angles.

Keywords: plasmon, gold nanoparticle, graphene oxide, angular scattering.



# Contents

<b>1</b>	<b>Introduction</b>	<b>2</b>
1.1	Purpose . . . . .	3
1.2	Limitations . . . . .	3
<b>2</b>	<b>Theory</b>	<b>4</b>
2.1	Rayleigh Scattering and Plasmon Resonance for Small Metal Spheres . . . . .	4
2.2	Mie Scattering . . . . .	5
2.3	Optical Response of Bulk Metals . . . . .	8
2.4	Plasmon Damping . . . . .	9
<b>3</b>	<b>Equipment</b>	<b>12</b>
3.1	Light Source and Optics . . . . .	12
3.2	Chamber . . . . .	13
3.3	Detection . . . . .	13
3.4	Vacuum System . . . . .	14
<b>4</b>	<b>Sample Preparation and Characterization</b>	<b>16</b>
4.1	Colloidal Gold Nanoparticle Sample . . . . .	16
4.2	Graphene Oxide Sample . . . . .	16
4.3	Mixed GO-AuNP Sample . . . . .	17
4.4	Characterization . . . . .	17
4.5	Geometry of Measurement . . . . .	20
<b>5</b>	<b>Results and Discussion</b>	<b>22</b>
5.1	Absorption Peak Shifts . . . . .	22
5.2	Plasmon Damping . . . . .	22
5.2.1	Radiative Damping . . . . .	25
5.3	Angular Measurements . . . . .	26
5.3.1	Angular Scattering Intensities . . . . .	26
5.3.2	Angular Absorption Spectrum . . . . .	30
<b>6</b>	<b>Conclusions and Outlook</b>	<b>42</b>



# Chapter 1

## Introduction

Plasmonic nanoparticles have been used by mankind for many years. They were used to tint glass in churches, and in other applications. The most famous is possibly Lycurgus cup [1]. The cup was created in 4th-century. The cup has a green color when light is reflected from its surface. When viewing the backside of the cup and the transmitted light, the cup looks red. This effect originates from the colloidal gold and silver nanoparticles. The romans certainly did not know what caused this effect. Light scattering by nanoparticles can also be observed in nature. The blue and red sky is a example of light scattering by nanoparticles. When the sun is high, Rayleigh scattering is caused in the atmosphere. The atmosphere contains molecules which scatter the light in all directions. The intensity of the scattered light depends on the wavelength. Shorter wavelengths has higher intensities, and the sky seems blue. Larger nanoparticles can also be found in the atmosphere. When the sun is just above the horizon, the light travels a larger distance in the atmosphere and interacts with more larger nanoparticles. Larger nanoparticles scatter differently compared to molecules, and starts to dominate over Rayleigh scattering when the sun is close to the horizon, which causes the red sky.

Light scattering occurs during the process when a nanoparticle is inside a propagating and oscillating electrical field, which causes the excitation of plasmons. The plasmon energy is dissipated through non-radiative decay, or radiative decay. Non-radiative decay is the absorption of the plasmon energy through electronic transitions in the material. Light scattering occurs when the plasmon oscillation is re-emitted.

Lately, knowledge about plasmonic nanoparticles has increased. This has led to many applications, such as light trapping for solar cells applications. Other important applications are; photodynamic therapy, where infrared absorbing plasmonic nanoparticles are used to kill cancer cells, sensor applications, for example hydrogen sensing in fuel cell cars; catalysis and many more applications [2].

The angular light scattering properties are obviously very important. If plasmonic nanoparticles are used in sensor applications, acquiring the signal where the nanoparticle scatters most is important.

The angular scattering of 60 *nm* in diameter gold nanoparticles are studied in this study. The nanoparticles are embedded in partially reduced graphene oxide flakes. Effects of

graphene oxide flakes are studied. Partially reduced graphene oxide flake solution contains non-conducting reduced graphene flakes, but also non-reduced graphene flakes. Graphene is a new and interesting material with good conductive properties.

## 1.1 Purpose

The purpose of the experiments is mainly performing angular resolved measurements on gold nanoparticles. Today mostly transmission measurements or dark-field microscopy is performed on plasmonic nanoparticles; angular resolved measurements can be an important addition to established methods.

The angular scattering intensities will be measured, and also the peaks in the scattering spectrum at different angles. The secondary aim is studying the effects of partially reduced graphene oxide flakes on the gold nanoparticles. The graphene oxide will be compared with a sample with no graphene oxide.

## 1.2 Limitations

The main limitations is usage of only gold as nanoparticles, in one size. The study will also only include the usage of one type of graphene oxide solution, and not several different graphene oxide solutions. There are limitations in sample preparations as well. The study will not include samples with different concentrations of graphene oxide or gold nanoparticles. Precise preparations in clean-rooms, will not be a part of the study.

## Chapter 2

# Theory

### 2.1 Rayleigh Scattering and Plasmon Resonance for Small Metal Spheres

The angular scattering distribution for infinitely small particles or molecules can be viewed in figure 2.3. The top figure illustrates Rayleigh scattering. The intensities of the Rayleigh scattered light depends on the wavelength as [3]:

$$I \propto I_0 \lambda^{-4} \quad (2.1)$$

If the incoming wavelength is considerably larger compared to the size of the particle, the particle will experience a static E-field  $E_0 \hat{\mathbf{x}}$ , where it is assumed that  $\hat{\mathbf{x}}$  is the direction of propagation. To determine the electrical field inside and around the particle, the Laplace's equation  $\nabla^2 \varphi = 0$  must be solved.  $\mathbf{E}$  is related to  $\varphi$  by  $\mathbf{E} = -\nabla \varphi$  [4]. The internal and external electrical field for small, but not infinitely small particles, is expressed by the following two equations [5]:

$$E_{internal} = E_0 \frac{3\epsilon_m}{\epsilon + 2\epsilon_m} \quad (2.2)$$

$$E_{external} = \hat{\mathbf{x}}E_0 - \alpha E_0 \left[ \frac{\hat{\mathbf{x}}}{r^3} - \frac{3\hat{\mathbf{x}}}{r^5} (\mathbf{x}\hat{\mathbf{x}} + \mathbf{y}\hat{\mathbf{y}} + \mathbf{z}\hat{\mathbf{z}}) \right] \quad (2.3)$$

The static polarizability  $\alpha$  is:

$$\alpha = 4\pi\epsilon_0 R^3 \frac{\epsilon - \epsilon_m}{\epsilon + 2\epsilon_m} = \alpha_{cl} g_d \quad (2.4)$$

Plasmon oscillation occurs when  $E_{internal}$  becomes very large, which it does when the condition  $\epsilon + 2\epsilon_m = 0$  is fulfilled. If the permittivity of the medium is assumed to be real, the plasmon excitation will occur for negative permittivity values for the small metal nanoparticles.

$$\epsilon_1 = -2\epsilon_m \quad (2.5)$$

The absorption efficiency ( $Q = Q_{ext} + Q_{sca} = \sigma/A$ ) is the following:

$$Q_{ext} = 4x \text{Im}(g_d) \quad (2.6)$$

$$Q_{sca} = \frac{8}{3} x^4 |g_d|^2 \quad (2.7)$$

, where  $x = 2\pi a \sqrt{\epsilon_m} / \lambda$ .

## 2.2 Mie Scattering

The Laplace equation was used for Rayleigh scattering, due to the particles small sizes. When using larger particles ( $>10\text{ nm}$ ), Helmholtz equation has to be used. The difference is the added term, which includes the wave vector. Very small particles experience a static electrical field; it is possible to use the Laplace equation for very small particles. Larger particles will experience a shifting field, which makes Laplaces' equation inaccurate for larger particles. Maxwell's equations can be used to describe light scattering [6].

$$\nabla \times \mathbf{E} = -ik\mathbf{H} \quad (2.8)$$

$$\nabla \times \mathbf{H} = ikm^2\mathbf{E} \quad (2.9)$$

The wave is assumed to travel through a homogeneous material with no currents or charges. Variable  $k$  is the wavenumber ( $k = \omega/c$ ), and  $m$  is the complex refractive index of the medium.

$$\nabla^2 \mathbf{A} + k^2 m^2 \mathbf{A} = 0 \quad (2.10)$$

, where  $\mathbf{A}$  is the potential.  $\psi$  is a scalar function, and the following equation must be satisfied:

$$\nabla^2 \psi + k^2 m^2 \psi = 0. \quad (2.11)$$

In spherical coordinates equation 2.11 has the following form:

$$\frac{1}{r^2} \frac{\partial}{\partial r} \left( r^2 \frac{\partial \psi}{\partial r} \right) + \frac{1}{r^2 \sin \theta} \frac{\partial}{\partial \theta} \left( \sin(\theta) \frac{\partial \psi}{\partial \theta} \right) + \frac{1}{r^2 \sin^2 \theta} \frac{\partial^2 \psi}{\partial \phi^2} + k^2 m^2 \psi = 0. \quad (2.12)$$

Vector functions are introduced to solve the wave equation [7]:

$$\mathbf{L} = \nabla \psi \quad (2.13)$$

$$\mathbf{M} = \nabla \times (\mathbf{r}\psi) \quad (2.14)$$

$$\mathbf{N} = \frac{1}{|\mathbf{k}|} \nabla \times \mathbf{M} \quad (2.15)$$

$\mathbf{L}$  represents the longitudinal wave, which for the dipolar mode can be set to  $\mathbf{L} = 0$  if the dipolar oscillation is assumed not to oscillate in the longitudinal direction.  $\mathbf{M}$  and  $\mathbf{N}$  are the curl of each other and follow equations 2.8 and 2.9. The extinction and scattering cross-sections are the following [7], [2]:

$$\sigma_{ext} = \frac{2\pi}{|\mathbf{k}|^2} \sum_{L=1}^{\infty} (2L+1) \text{Re}(a_L + b_L) \quad (2.16)$$

$$\sigma_{sca} = \frac{2\pi}{|\mathbf{k}|^2} \sum_{L=1}^{\infty} (2L+1) (|a_L|^2 + |b_L|^2) \quad (2.17)$$

, where

$$a_L = \frac{m\psi_L(mx)\psi'_L(x) - \psi'_L(mx)\psi_L(x)}{m\psi_L(mx)\eta'_L(x) - \psi'_L(mx)\eta_L(x)} \quad (2.18)$$

$$b_L = \frac{\psi_L(mx)\psi'_L(x) - m\psi'_L(mx)\psi_L(x)}{\psi_L(mx)\eta'_L(x) - m\psi'_L(mx)\eta_L(x)} \quad (2.19)$$

,  $m = n/n_m$ ,  $n$  is the complex index of refraction and  $n_m$  is the index for the surrounding medium.  $\psi_L$  and  $\eta_L$  are Riccati-Bessel cylindrical functions [7]. Index  $L$  is the order of the partial wave.  $L = 1$  is a dipole,  $L = 2$  is a quadrupole and so forth. The extinction by infinitely small particles is only affected by the dipole mode. As the size of the particle increases higher modes starts to contribute. The Mie-extinction consists of the contribution of several modes. This is illustrated in figure 2.1. The 60 nm spherical gold particles used in this experiment will have the characteristic between small particles and Mie particles. The quadrupolar mode will become a significant contribution at 40 nm particle sizes, and will dominate over the dipolar mode at 60 nm sizes. Figure 2.2 shows the electrical and magnetic fields inside the particle for the first three modes.

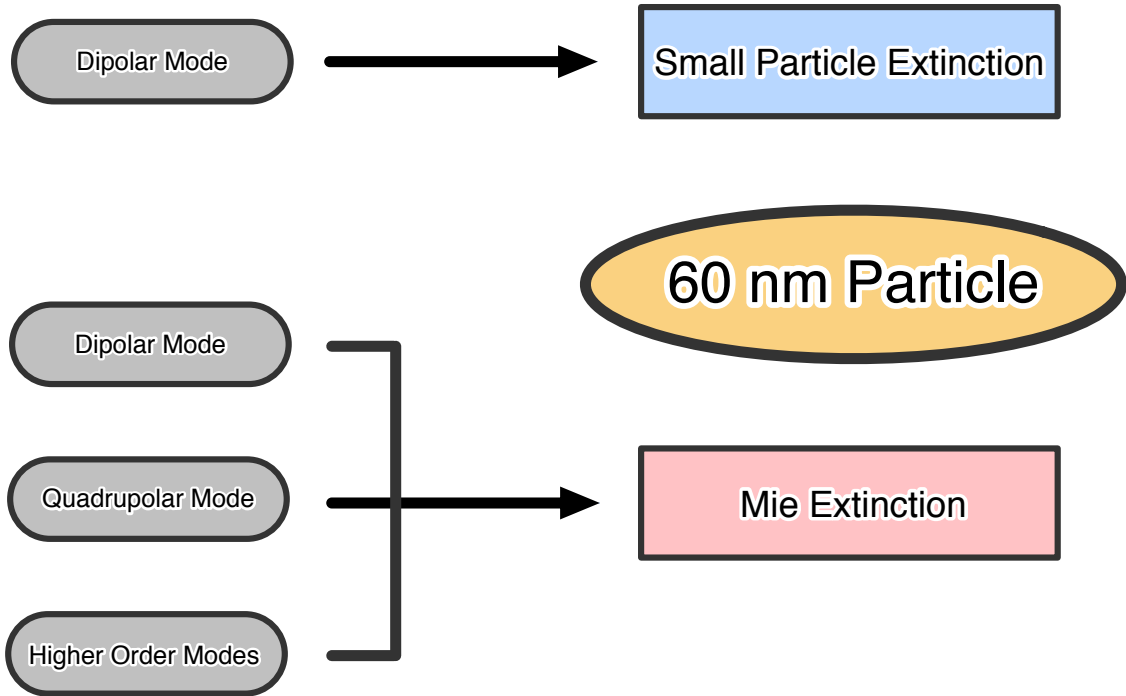


Figure 2.1: The dipolar mode is the only contribution in small particle extinction. For larger particles, modes of higher order starts to contribute to the extinction. 60 nm particles, used in the measurements, is in between the two regions.

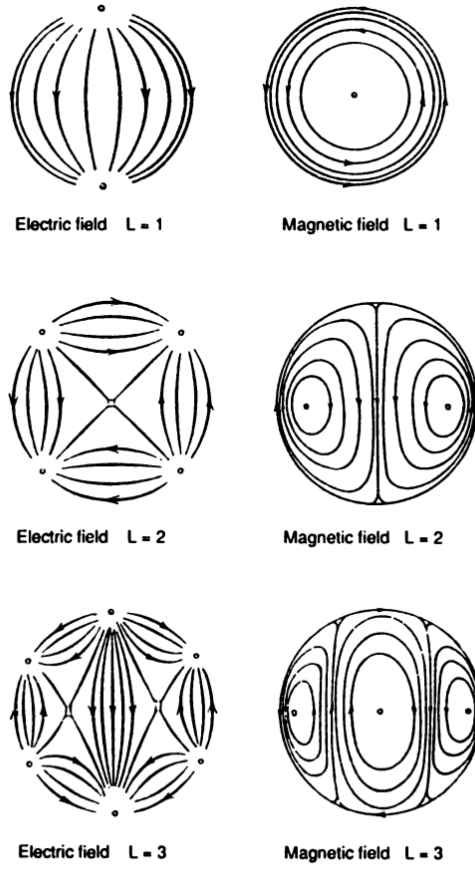


Figure 2.2: The picture shows the electrical and magnetical fields for  $L = 1, 2, 3$ . The dipolar mode is the only contribution for small particles. For larger particles, higher modes are involved for the electron oscillations. Picture taken from [7]

The dielectric environment will affect the plasmon resonance frequency, which is described as [7]:

$$\omega_1 = \frac{\omega_p}{\sqrt{1 + 2\epsilon_m}} \quad (2.20)$$

The equation above is only valid for dipole modes. Larger particles, which will be used in the experiments will also have plasmon oscillation in a quadrupolar mode. The resonance frequency for higher multipole orders is slightly different, and is [7]:

$$\omega_L = \frac{\omega_p}{\sqrt{1 + \frac{1+L}{L}\epsilon_m}} \quad (2.21)$$

The scattering characteristic will change as different modes start to contribute. Figure 2.3 shows the angular scattering for particles with three different sizes.

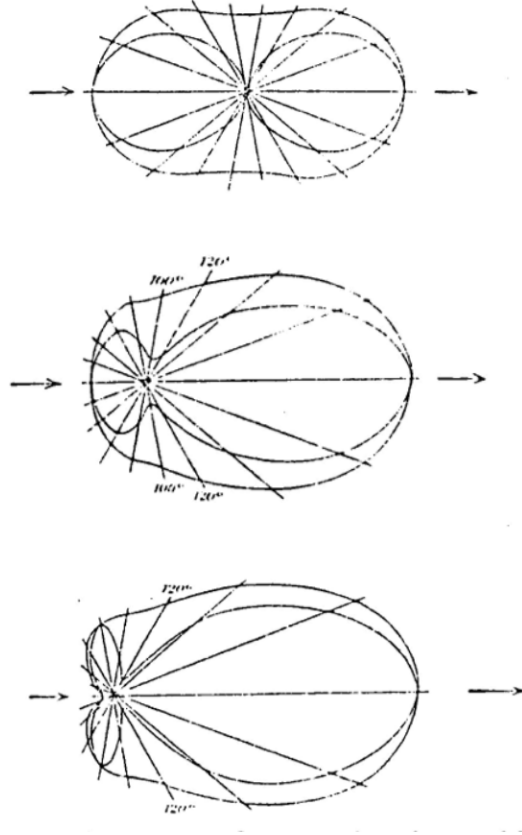


Figure 2.3: The figure shows the angular scattering of three different sized particles. The top figure is representing a infinitely small particle. The middle figure represents the angular scattering of 160 nm particles, and the bottom figure represents 180 nm large particles. As the size of a particle increases, the intensity of the back scattered light increases. Picture taken from [8].

## 2.3 Optical Response of Bulk Metals

To describe how an external electrical field affects a metal bulk material, the electrons can be assumed to be free electrons. The Drude-Lorentz-Sommerfeld model can be used, which describes how a free electron responds. The response to the external field  $\mathbf{E} = \mathbf{E}_0 e^{-i\omega t}$  is [7]:

$$m_e \frac{\partial^2 \mathbf{r}}{\partial t^2} + m_e \Gamma \frac{\partial \mathbf{r}}{\partial t} = e E_0 e^{-i\omega t} \quad (2.22)$$

, where  $\Gamma$  is the damping constant. By solving equation 2.22, the displacement of an electron as a function of the incident wave frequency is obtained.

$$\mathbf{r}(\omega) = -\frac{e}{m_e} \frac{\mathbf{E}_0 e^{-i\omega t}}{\omega^2 + i\omega\Gamma} \quad (2.23)$$

The dipole moment is defined as  $\mathbf{p} = e\mathbf{r}$ . By adding all electrons the total dipole moment  $\mathbf{P} = n\alpha\mathbf{E}$  is obtained. The total dipole moment can also be described as:  $\mathbf{P}(\omega) =$

$\epsilon_0 \chi \mathbf{E}(\omega)$ , where  $\epsilon(\omega) = 1 + \chi(\omega)$ . From these expressions, the complex dielectric function can be written as [7]:

$$\epsilon(\omega) = 1 - \frac{\omega_p^2}{\omega^2 + i\Gamma\omega} = 1 - \frac{\omega_p^2}{\omega^2 + \Gamma^2} + i \frac{\omega_p^2 \Gamma}{\omega(\omega^2 + \Gamma^2)} \quad (2.24)$$

, where  $\omega_p = \sqrt{\frac{ne^2}{\epsilon_0 m_e}}$  is the Drude plasma frequency, which is not excited by light in the bulk material. For free electrons  $\omega \gg \Gamma$ , and the real and imaginary parts of the dielectric function  $\epsilon = \epsilon_1 + i\epsilon_2$  are:

$$\epsilon_1(\omega) \approx 1 - \frac{\omega_p^2}{\omega^2}, \quad \epsilon_2 \approx 1 - \frac{\omega_p^2}{\omega^3} \Gamma \quad (2.25)$$

If  $\omega = \omega_p$ , then  $\epsilon_1 = 0$ , which is the condition, if the frequency of the electrons is going to match the plasma frequency.

The electrical field inside a bulk metal will depend on the depth in the bulk material, due energy loss of the propagating wave.

$$\mathbf{E}(\mathbf{r}, t) = \mathbf{E}_0(\mathbf{r}, t) e^{i\omega(zn_r/c - t)} e^{-z/\delta} \quad (2.26)$$

, where  $\delta = \lambda/2\pi k$  is the skin depth.  $k$  is the absorption coefficient.

## 2.4 Plasmon Damping

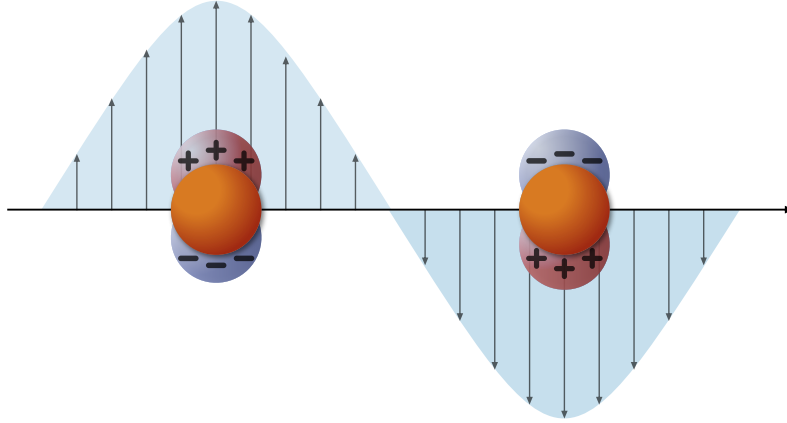


Figure 2.4: Oscillation of the electron cloud inside a metal nanoparticle, due to a propagating and oscillating electrical field. The atom cores and its inner electrons are stationary, and the outer electrons move freely. The arrows represent the E-field, which is defined as the flow going from positive to negative charges.

Plasmon resonances can be described by damped harmonic oscillators. The motion follows [9]:

$$x(t) = e^{-\gamma t} A \cos(\omega_1 t + \phi) \quad (2.27)$$

, which describes a under dampened motion. Here,  $\phi$  is the phase shift,  $\gamma$  is the damping parameter and  $\omega$  is the angular frequency.  $A$  depends on the boundary conditions.

The damping parameter will determine the width of the peak, and a damped plasmon oscillation will have the shape of a Lorentzian function.

$$L(x) = \frac{1}{\pi} \frac{\frac{1}{2}\Gamma}{(x - x_0)^2 + (\frac{1}{2}\Gamma)^2} \quad (2.28)$$

, where  $x_0$  is the position of the peak and  $\Gamma$  is the FWHM. A undamped plasmon oscillation will instead follow a Gaussian function.

$$f(x) \approx \frac{1}{0.425\Gamma\sqrt{2\pi}} e^{-(x-x_0)^2/(0.361\Gamma^2)} \quad (2.29)$$

There are different types of dampening effecting the plasmon oscillation. One type is radiative damping. Electrons can lose a portion of their energy during oscillation through radiation. The force of the decelerative radiation is proportional to [5]:

$$R \propto \sqrt{\epsilon_m}(1 + L(\epsilon/\epsilon_m - 1)) \quad (2.30)$$

, where  $L = 1/3$  for spherical particles [10] and  $\epsilon \approx 10$  for gold at  $\lambda \approx 600 \text{ nm}$  [12]. Note that this is the force of a dipole, and will be accurate for smaller particle sizes. For larger particle sizes the higher modes are more important.

Another reason for damping is electron scattering. Electrons can scatter at phonons, lattice defects etc. The electron scattering effect becomes significant when the electron free path is comparable to the particle size [7].

The damping affects the peak shape, but also affects the peak width. The width of the peak is given by [7]:

$$\Gamma = \frac{2\epsilon_2}{(\frac{d\epsilon_1}{d\omega})^2 + (\frac{d\epsilon_2}{d\omega})^2} (1 + \beta) \quad (2.31)$$

, where  $\epsilon_1$  and  $\epsilon_2$  are the real and imaginary part of the dielectric function, and  $\beta(\omega_{max}, \epsilon_2, d\epsilon_1/d\omega, d\epsilon_2/d\omega)$ . The width of the plasmon peak is affected by the varying dielectric constant over different frequencies. In figure 2.5, a constant dielectric function over a span of frequencies leads to peak broadening.

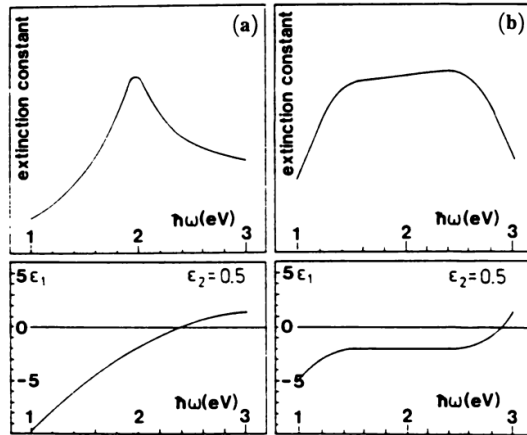


Figure 2.5: Two peaks with different dielectric properties. A constant dielectric function leads to peak broadening. Picture taken from [7]



## Chapter 3

# Equipment

### 3.1 Light Source and Optics

Lasers could be used to illuminate the samples and measure the scattered light. The disadvantage with lasers is the range limitation in wavelength. Instead a *UV*-lamp was used, which covered *UV* to *VIS* range. The advantage with *UV*-lamps was the possibility to cover a large wavelength span in one measurement.

Apertures and lenses were used to obtain a homogeneous light beam. Image of the lamp was projected onto a screen during focusing of the light beam. The lamp image, as mentioned, was removed by the usage of apertures and lenses.

The *UV*-light source consisted of a power supply, a lamp housing, a *IR* water filter and, as mentioned, several apertures and lenses.

Lamp housing model A-1010B by OBB was used in the experiments. It was a sealed housing, so it was containing ozone gases from escaping. The tubular lamp was mounted halfway through an ellipsoidal mirror, which was used to focus the outgoing light. The lamp igniter was designed not to emit any radio waves. The type of *UV*-lamp used was a 75 W Xenon-lamp. One advantage by using a Xenon-lamp was its continuous spectrum, compared to Xenon-Mercury lamps. A *IR* water filter was used to filter out any heat emitted by the *UV*-lamp. The filter was simply a container with quartz windows at the ends. The container consisted of an inner container and an outer shell. Distilled water could flow between the surfaces of the two tubes and cool the distilled water, contained by the inner tube. The *IR* filter transmitted light above 200 nm and blocked light above 1000 nm. Two lenses and three apertures were used to focus a smaller, homogeneous beam onto the sample. The first aperture was blocking the wide beam of light, which spread outside the first lens. The first lens was then used to focus the light onto a second aperture. Internal parts of the lamp housing were visible after the first lens. The second aperture was used to achieve a projected beam of light without any non-homogeneous features onto the sample. Due to the setup, the *UV*-lamp was not close enough to the sample to obtain a smaller beam onto the sample with higher intensity. Therefore a second lens was used to collect and focus the light from the second aperture onto the sample. A third aperture was used to block any excess light. The first and third apertures were not crucial but prevented unnecessary light from being reflected by the surrounding chamber walls, which could have

affected the measurements.

The true intensity of the incident light was measured with a Molectron 3SIGMA, connected to a PS10Q Powersens Probe.

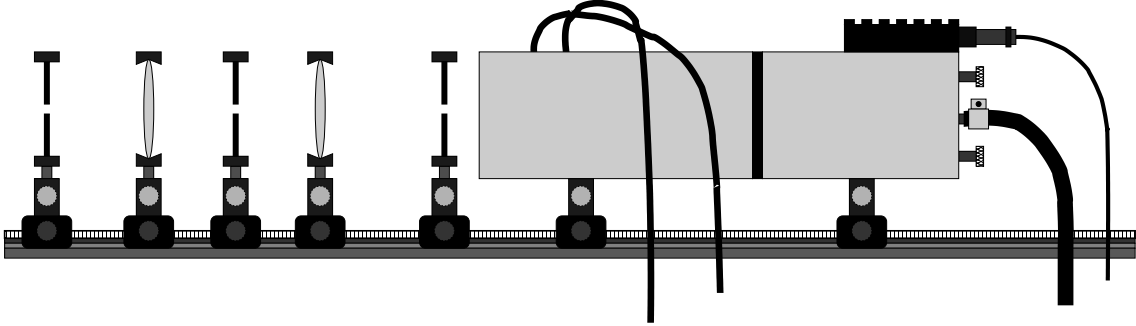


Figure 3.1: A figure of the UV light source setup. The UV-lamp is located at the far right of the picture and it is connected to a IR-filter, which is just in front of the lamp. Water hoses are connected to the lamp and IR-filter for cooling purposes. Knobs which adjusts a mirror are located at the back of the lamp. Unnecessary light is first screened away by the first aperture. The following two lenses and one aperture focuses the light and removes the image of the UV-lamp. The last aperture further removes unnecessary light.

## 3.2 Chamber

Measurements were performed inside a spherical vacuum chamber. The light source was aimed into the vacuum chamber, through viewports. The chamber had four viewports in the plane of the incident light. The viewports were VP-UV-C40 fused silica viewports from Caburn-MDC Europe Limited, which had a transmission range of 200  $nm$  to 2000  $nm$ . A  $Z$ -manipulator was connected to the top part of the chamber, which added the possibility of rotating the sample around one axis inside the chamber. The chamber used was the MCF275-SphCube-C6A8 from Kimball Physics Incorporation. It was a spherical chamber constructed out of 316L stainless steel. The chamber had a small pumping volume of 397  $cm^3$ , which is preferable during vacuum pumping. The vacuum chamber had eight measurement points where it was possible to connect fiber cables for measurements. The eight measurement points are located in a  $45^\circ$  angle relative to the center point of the spherical chamber. In practice the chamber had two planes of measurement points.

## 3.3 Detection

The spectrometer used for the spherical vacuum chamber is a Mightex ISP-VIS-MC006-A spectrometer. The spectrometer has six channels, and can detect a spectrum ranging from 380  $nm$  to 780  $nm$  with a resolution of 1.2  $nm$ .

A quadrupole mass spectrometer was connected to the vacuum system, which could detect the environment inside the chamber. The mass spectrometer could detect 0-300  $amu$ , and the measured environment inside the vacuum system can be seen in table 3.1.

Samples are characterized in a Cary 5000, which covers the wavelengths 175-3300  $nm$ .

$Ar$	$CO_2$	$H_2$	$H_2O$	$C_xH_y$	$N_2/CO$	$O_2$
5444.716 ppm	9.321 %	9.669 %	23.275 %	2.002 %	50.201 %	4.987 %

Table 3.1: Mass spectrometer measurement showing the contained gases inside the vacuum system.

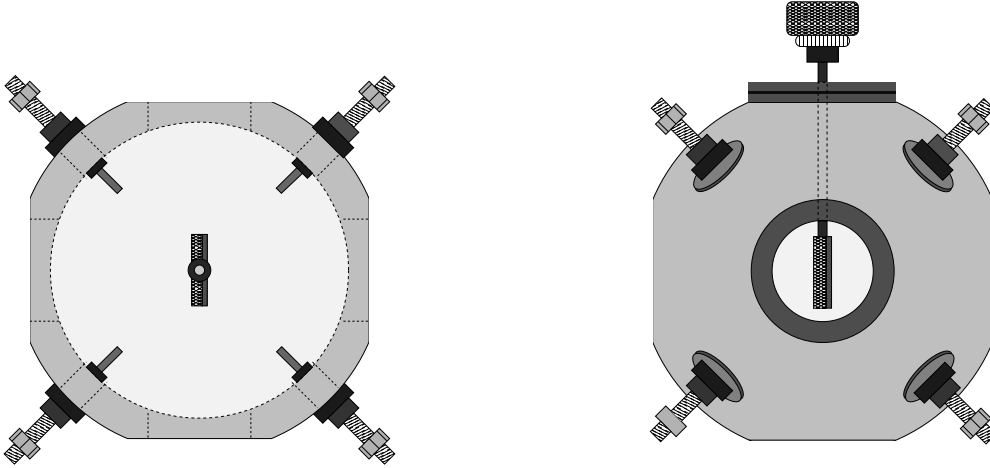


Figure 3.2: Two figures showing the vacuum chamber at different angles. The left figure is the top view of the chamber, and the right figure is the side view. A sample is put in the center of the chamber for measurements. The sample is fixed to a manipulator from the top, which can be used to rotate the sample inside the chamber. Around the chamber there are eight measurement points, which fiber-optic cables can be connected to. The measurement points have an equal distance to the sample and are angled equally relative to the sample.

### 3.4 Vacuum System

The spherical chamber is connected vacuum system. In addition, the system adds the possibility to change the environment through gas inlet ports.

The bottom part of the chamber is connected to a 6-way cross, with a straight connector, which both come from Vacuum Generators Limited. The straight connector has an outer bore diameter of  $43\text{ mm}$ , and has a wall thickness of  $1.63\text{ mm}$ . The straight connectors are ultra high vacuum compatible, and are made of 304L stainless steel. The 6-way cross is also made of 304L stainless steel and connects the chamber to the vacuum system, a mass spectrometer, a pressure sensor and a gas inlet valve to the vacuum chamber. The vacuum system is connected to the 6-way cross, with a straight connector, which has a diameter of  $38.2\text{ mm}$ . The vacuum system consists of two pumps, one mechanical fore-pump and one turbo pump. The used turbo pump is a Varian Turbo-V 250. The pumping volume is 250 liters of nitrogen per second. The blades rotate at  $56000\text{ rpm}$  and achieves a base pressure of  $2 \cdot 10^{-10}\text{ mbar}$ . According to standard DIN 28 428; the base pressure is the pressure after 48 hours of operation in a leak-free chamber. The fore pump is a  $130\text{ W}$  AEG rotary vane pump of type AMEB 71 NX2 R3 Y11 Q4 VDE0530/91, operating at  $2800\text{ rpm}$ . The rotary pump is connected to the bottom part of the turbo pump.

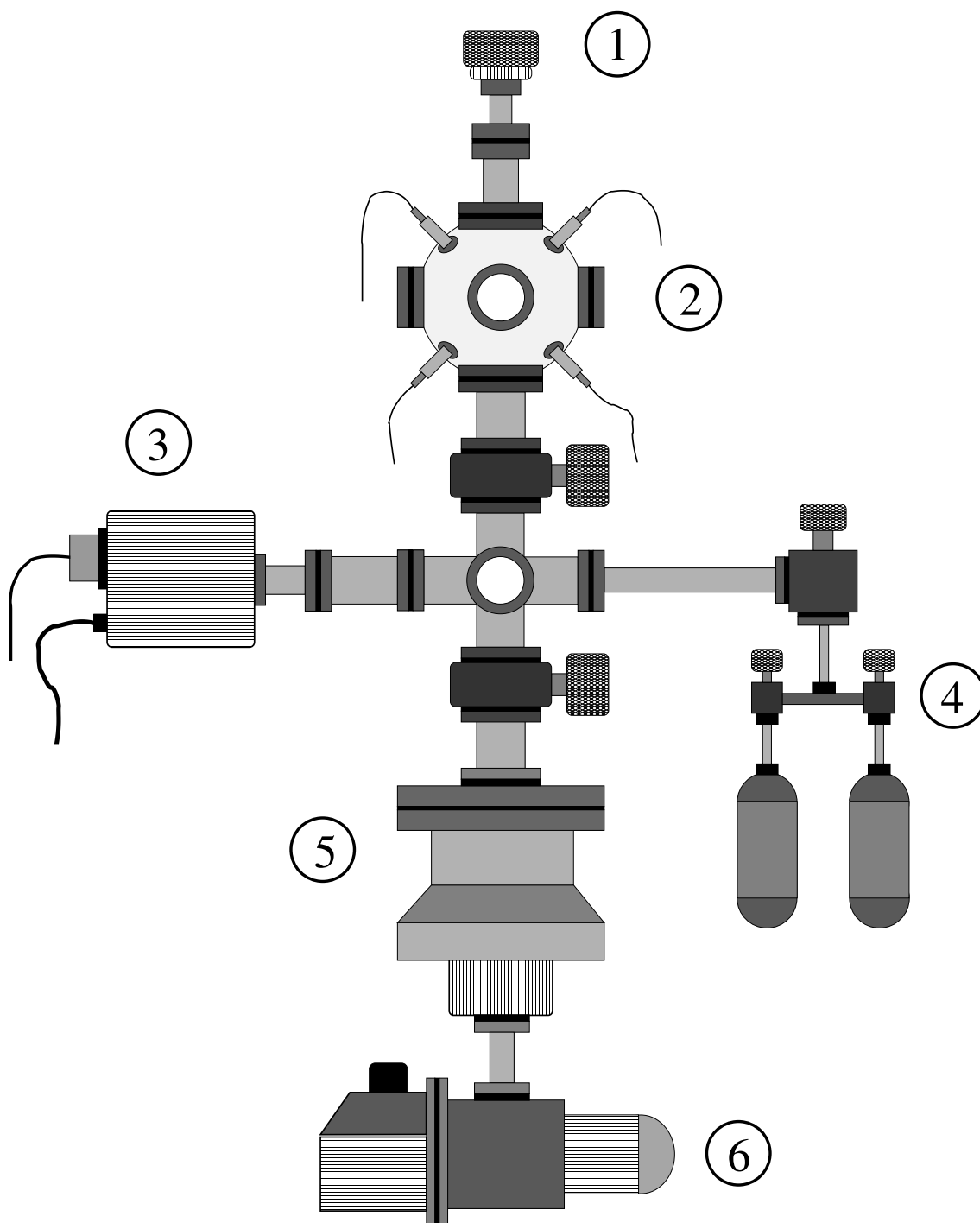


Figure 3.3: The vacuum system is shown in this figure. The Z-manipulator was located at the top, labeled as number 1. Beneath the manipulator was the spherical chamber where the sample would be measured on. A total of eight channels could be connected to the chamber. Only four channels are visible in the figure, the other four channels were located on the backside of the figure. At label number 3 was the mass spectrometer, and at label number 4 was the gas input system. Different gases could be inserted into the chamber through a valve where gas tubes of my choice could be attached. At number 5 was the high vacuum turbo pump, and at number 6 was the rotary vane vacuum pump.

## Chapter 4

# Sample Preparation and Characterization

Three different samples were used; samples with only graphene oxide, only gold nanoparticles and a sample with graphene oxide and colloidal gold nanoparticles mixed. Fused silica with a thickness of  $500\ \mu\text{m}$  were used as substrates.

### 4.1 Colloidal Gold Nanoparticle Sample

Colloidal gold nanoparticle solution was bought from Sigma-Aldrich. The *AuNPs* had a size of  $60\ \text{nm}$  and were dispersed in a citrate buffer, with a concentration of  $\approx 1.9\ \text{particles/mL}$ . Immobilization of the colloidal nanoparticles on fused silica substrates was attempted, but unsuccessful. The *AuNP* solution applied on bare substrates and later dried at  $50\ ^\circ\text{C}$  for  $60\ \text{min}$ . This did not make the *AuNP* stick to the substrate. A second attempt was made by charging the substrates. The citrate solution gives the nanoparticles a negative charge [11]. In order for the gold nanoparticles to stick to the surface, the substrate was covered by *PDDA*, which gave the surface a positive charge. Substrates were cleaned with ethanol. The substrates were rinsed in distilled water and blow dried. A concentration of  $0.2\ \%$  *PDDA* was applied on the substrate for  $15\ \text{min}$ . After the *PDDA* stage, the substrate was rinsed with distilled water and blow dried with nitrogen. Solution of colloidal gold nanoparticles was applied on the charged substrate and dried as previously, but still unsuccessful. The concentrations were enough for characterization in *Cary 5000*, but not enough for angular resolved measurements.

### 4.2 Graphene Oxide Sample

The graphene oxide was bought from Graphene Supermarket. The *GO*, dispersed in a aqueous solution, had a very high concentration of  $6.2\ \text{g/l}$ . The sizes of the *GO* flakes ranged between  $0.5$  and  $5\ \mu\text{m}$ . The *GO* solution was mixed with distilled water in a 1 to 1 ratio, applied on substrates and dried at  $50\ ^\circ\text{C}$  for  $60\ \text{min}$ .

### 4.3 Mixed GO-AuNP Sample

The *GO-AuNP* sample was manufactured by mixing the *GO*-solution and colloidal gold nanoparticles in a 1 to 2 ratio. The mixture was applied onto the substrate by using a pipette. The sample was dried at  $50^{\circ}\text{C}$  for  $60\text{min}$ . Figure 4.1 shows a example of how the sample could look like. The surface structure will be dependent on the pH of the solution, which the graphene oxide flakes are suspended in [13], [14].

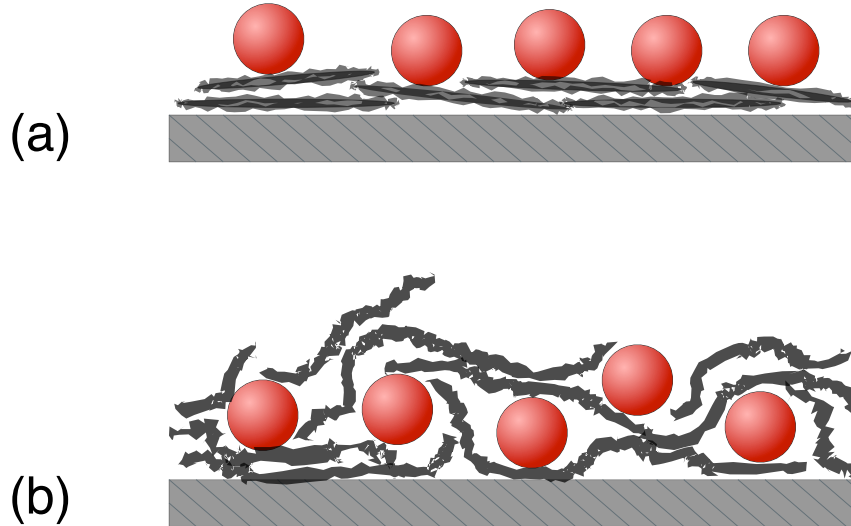


Figure 4.1: The top drawing (a) would be a ideal sample with nanoparticles on top of a layer of graphene oxide flakes. Difficulties in immobilization of gold nanoparticles led to the manufacturing of a sample with nanoparticles and flakes mixed. The shape the graphene flakes depends on the pH of the solution [13]. In order to confirm this figure, SEM images are needed, which were not taken. The length of the GO flakes are probably much larger compared to the relative sizes in this figure, since the flakes have sizes of a few  $\mu\text{m}$  and the particles are only  $60\text{nm}$  in diameter.

### 4.4 Characterization

The samples were characterized in a *Cary 5000* spectrophotometer, between the wavelengths  $375$  and  $800\text{nm}$ . These wavelengths were the limits of the 6-channel Mightex spectrometer, used in the spherical vacuum chamber. The samples and bare fused silica substrates were measured. The data from the samples were subtracted of the substrate contribution.

The result of the colloidal gold nanoparticle solution can be seen in figure 4.2. The peak position is at the wavelength of  $541\text{nm}$ , which is close to the specified value from the manufacturer of  $540\text{nm}$ . The graph in figure 4.3 was the result from the gold nanoparticles on fused silica substrate. The peak was shifted towards  $551\text{nm}$ . Lastly, figure 4.5 shows the peak from the particles mixed with graphene oxide flakes. The peak shifts due to change in dielectric environment is coherent with other studies where peak shifts for gold nanoparticles are observed for changing dielectric environment [15].

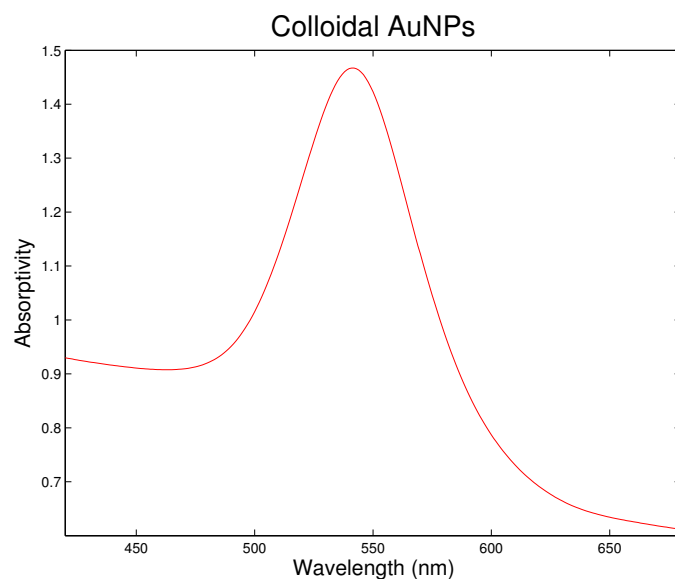


Figure 4.2: Plot showing the absorptivity for colloidal gold nanoparticles. The peak was at 541 nm and the FWHM = 50.9 nm.

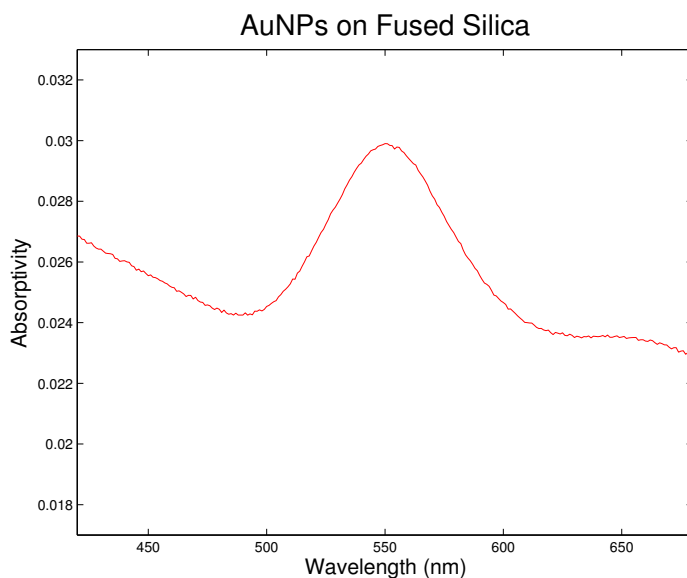


Figure 4.3: Plot showing the absorptivity for gold nanoparticles on fused silica substrate. The peak was at 551 nm and the FWHM = 54.5 nm.

The graphs above show the absorptivity for the different samples. The angular graphs are also important, and therefore it was important for the two spectrometers to show the same result when measuring on the same sample during similar setup. Figure 4.6 shows the comparison between two absorptivity measurements for a colloidal gold sample. The peaks were very similar between the two spectrometers. For the 6-channel Mightex a peak at 539 nm was measured. Using the Cary 5000, a peak at 541 nm was measured.

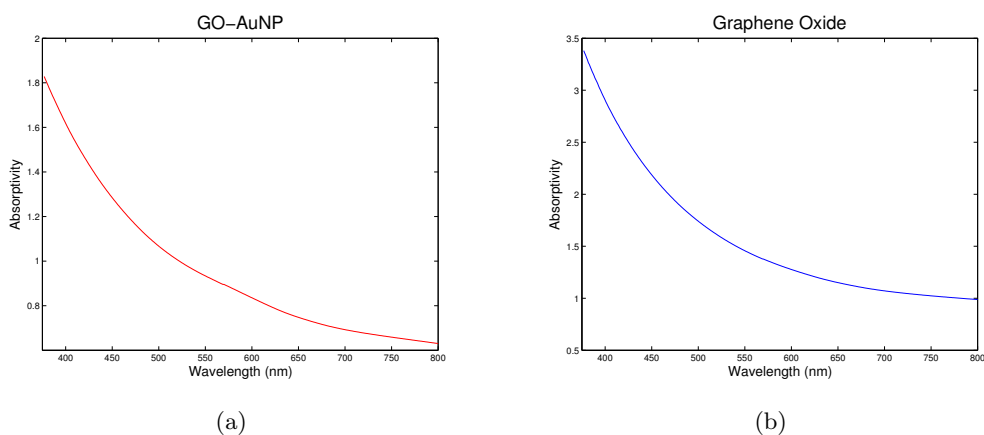


Figure 4.4: The absorption spectrum of graphene oxide is shown in the right figure, and the left figure is the absorptivity of graphene oxide mixed with gold nanoparticles.

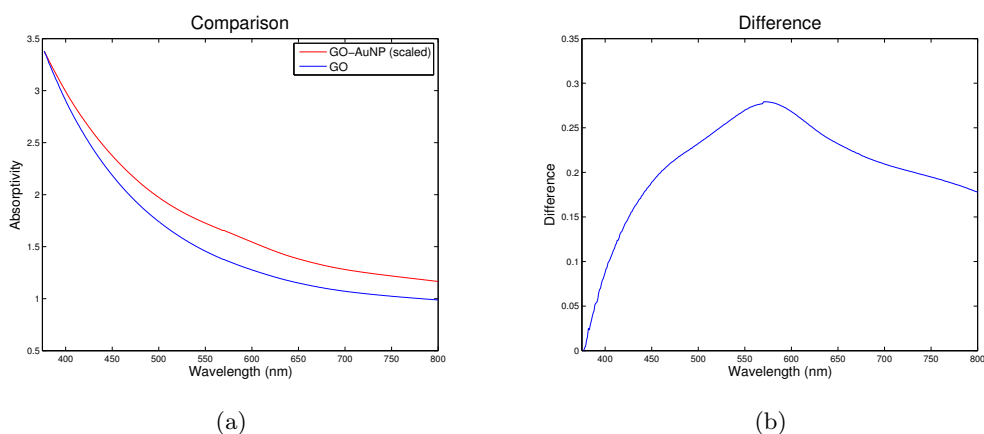


Figure 4.5: The two curves from figure 4.5 is normalized at the smallest wavelength and compared at the left figure. The right figure shows the difference of the two curves at the left. The peak wavelength is 573 nm and the width is 127.3 nm.

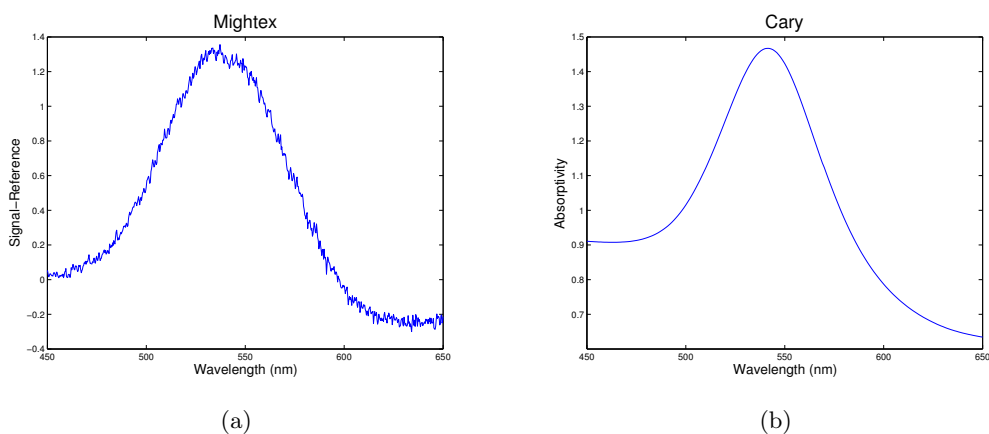


Figure 4.6: The two graphs shows the absorption spectrum from the two spectrometers used in the experiment. Cary 5000 was used for characterization and 6-channel Mightex was used during angular measurements. The Mightex has a peak at 539 nm and the Cary 5000 shows a peak at 541 nm.

## 4.5 Geometry of Measurement

The geometry of the measurements are important, since different scattering peaks are expected at different angles [22] and the common techniques do not cover all angles.

For each measurement data from eight angles were obtained. By rotating the sample for every new measurement, all angles could be covered. By using all channels, it was possible to perform measurements covering  $360^\circ$  of the sample by just rotating in total  $90^\circ$ . The incident light-beam covered the whole sample, to keep the number of interacting particles constant during rotation. The cross-section of partially covering beams would change during rotation of the samples.

The chamber had windows on four sides, which were kept open to avoid reflected light. The measurements were conducted in a spherical vacuum chamber, at atmospheric pressure. The light intensity from the *UV*-lamp was measured before each measurement series. The input power of the *UV*-lamp was  $56\text{ W}$  for all measurements. The apertures were adjusted for the different samples in order for the light beams to just cover the differently sized samples. The true light intensity was  $\sim 2\text{-}7\text{ mW}$ , depending on aperture settings. The samples were measured with a angular resolution of  $5^\circ$ . The exposure of each measurement was  $6900\text{ ms}$ , and 15 averages were used. The spectrometer had six channels available, but only four were used. The channels covered one side at the time, front or back. The sample was rotated so the four channels would cover all angles, at two planes, on one side.

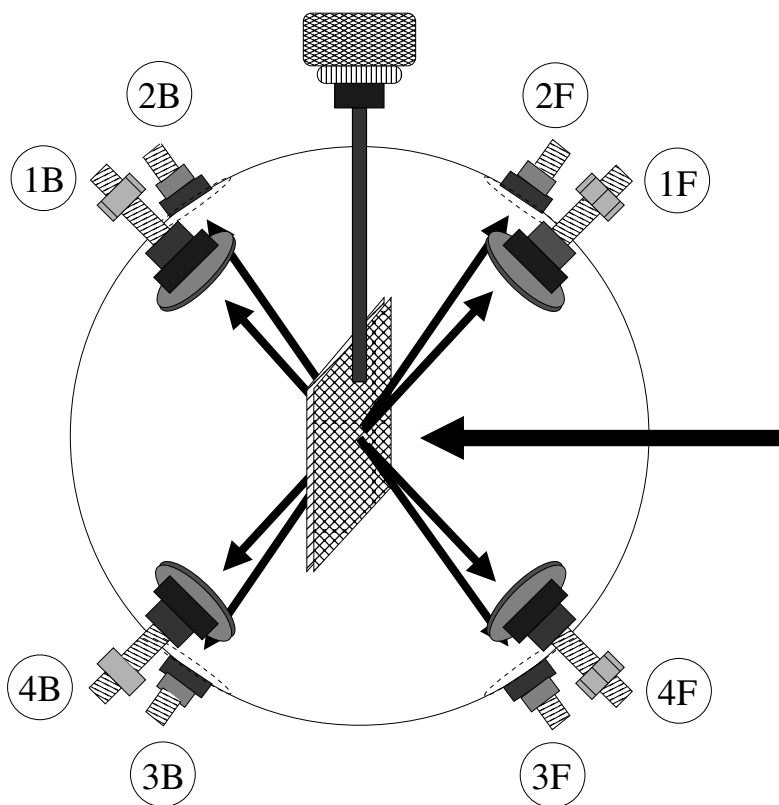


Figure 4.7: This figure shows the principle of the measurements. A sample was located inside the spherical chamber, which could be rotated. The incoming light beam from a UV source was impinging on the surface. The scattered light was collected by the surrounding measurement points.

## Chapter 5

# Results and Discussion

### 5.1 Absorption Peak Shifts

Figure 5.1 compares the absorption peaks for gold nanoparticles in different surrounding medium. These shifts were caused by changes in the dielectric environment. The colloidal gold, which was suspended in a citric buffer, had a peak at  $541\text{ nm}$ . When the colloidal gold droplets were applied on a fused silica substrate, the peak shifted to  $550\text{ nm}$ . The peak for the gold nanoparticles mixed with graphene oxide showed a further shift in absorptivity peak, which was at  $573\text{ nm}$ .

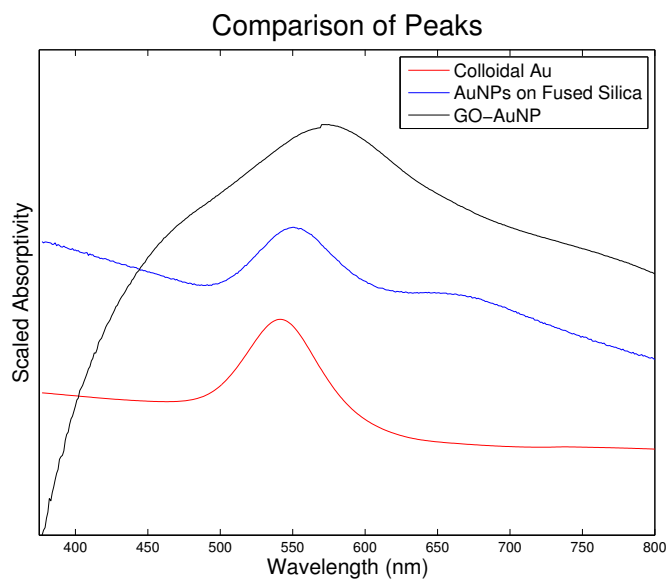


Figure 5.1: The figure shows the absorptivity peak comparison between colloidal gold nanoparticles, gold nanoparticles on fused silica and gold nanoparticles mixed with graphene oxide flakes.

### 5.2 Plasmon Damping

It was interesting to study the shape of the peaks, which revealed information about the particles and the surrounding medium. Plasmon peaks have the shapes depending if the electron oscillations are damped or un-damped. A un-damped oscillation has a

peak shape of a Gaussian function. A dampened oscillation will have a peak shape similar to a Lorentzian function. Damping can be caused by several factors. The most likely factors are radiative dampening, electron scattering or other types of damping caused by lattice impurities etc. The absorption peak of the colloidal gold nanoparticles was fitted to the Gaussian function, which can be seen in figure 5.2. The colloidal gold nanoparticles were most likely un-dampened in the citric solution. Figure 5.3 shows the peak from gold nanoparticles on fused silica, which was fitted to a Gaussian function.

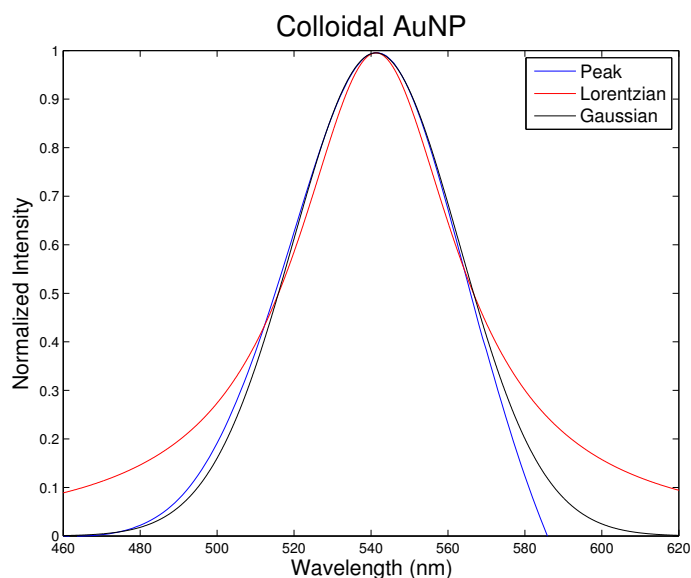


Figure 5.2: A graph of the colloidal gold nanoparticle absorption peak with a Gaussian and Lorentzian function fitted to the peak. The Gaussian function is the best fit. The peak is at wavelength 541 nm and the half height width of the peak is 50.9 nm.

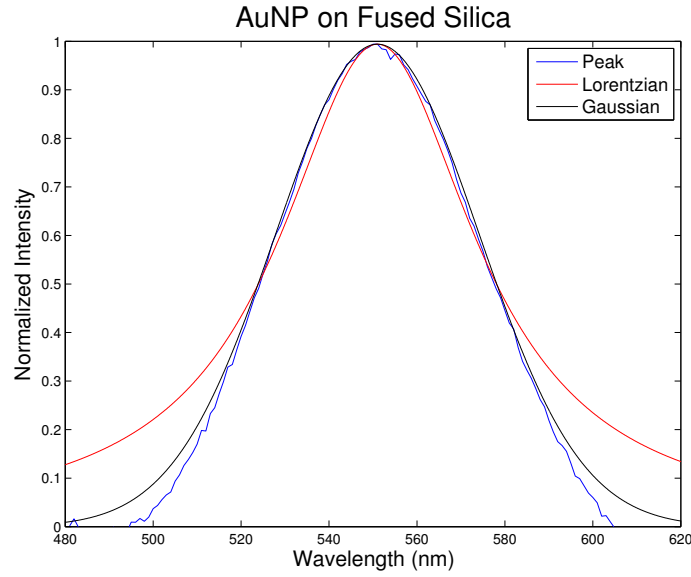


Figure 5.3: A graph of the absorption peak from gold nanoparticles on fused silica substrate with fitted Gaussian and Lorentzian functions. The Gaussian function is the best fit. The peak is at wavelength 551 nm and the half height width of the peak is 54.5 nm.

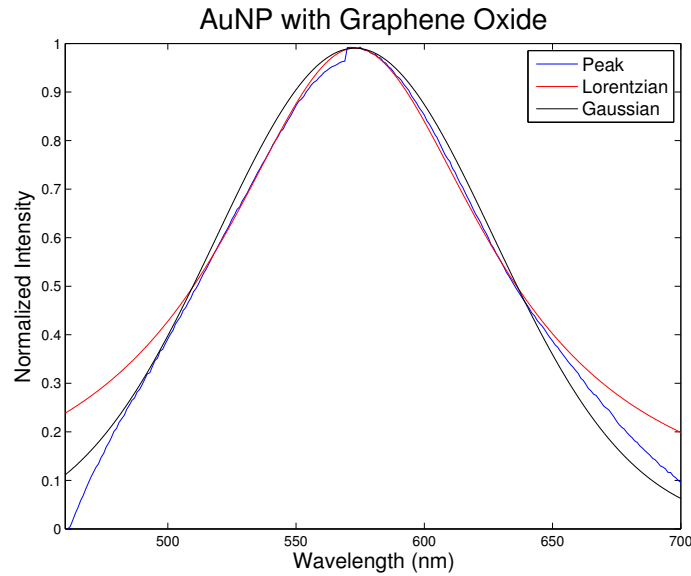


Figure 5.4: The absorption peak of the graphene oxide gold nanoparticle mix with Gaussian and Lorentzian function fit. Lorentzian function is the best fit. The peak is at wavelength 573 nm and the half height width of the peak is 127.3 nm.

However, the peak for the gold nanoparticles embedded in graphene oxide flakes, was dampened. The peak fitted with the Lorentzian function. The peak for the *GO-AuNP* sample was derived from the difference between two samples, with *AuNPs* and without. The absorptivity curves for the two samples did not fit each other after linear scaling. This difference led to a deformed peak foot for the *GO-AuNP* absorptivity peak. The bottom

part seemed to fit better with the Gaussian, but as previously explained, the foot of the peak was deformed, which can be viewed in figure 4.5. The upper part of the peak was more interesting, which fitted with the Lorentzian. The plasmon oscillation was clearly dampened by the surrounding graphene oxide flakes.

### 5.2.1 Radiative Damping

One of the reasons for the dampening of the plasmon peak for the graphene oxide gold nanoparticle sample could be radiative dampening. The blue curve in figure 5.5 is proportional to the force of radiative damping for an oscillating dipole. The value of the red line is proportional to the radiative force at the dielectric constant of water, which is 1.77. The red line represents the colloidal solution, which consisted of a citrate buffer, but was assumed to have the dielectric properties of water. The black line represents the fused silica. The dielectric constant of fused silica is 2.25 [17]. If the reason for the Lorentzian fit was dipolar radiative dampening, the value for the blue curve should be higher than the red and black curves at the dielectric constant of 2.75 [18], which is the constant for graphene oxide. The dampening force increases for larger dielectric constants. According to this model, the dielectric constant must be much larger compared to 2.75 [?], if dipolar radiative dampening was the main cause of the dampening. This model only represents the radiative dampening for dipolar modes. A quadrupolar mode is present for 60 nm particles, which the model for dipolar radiative dampening does not include.

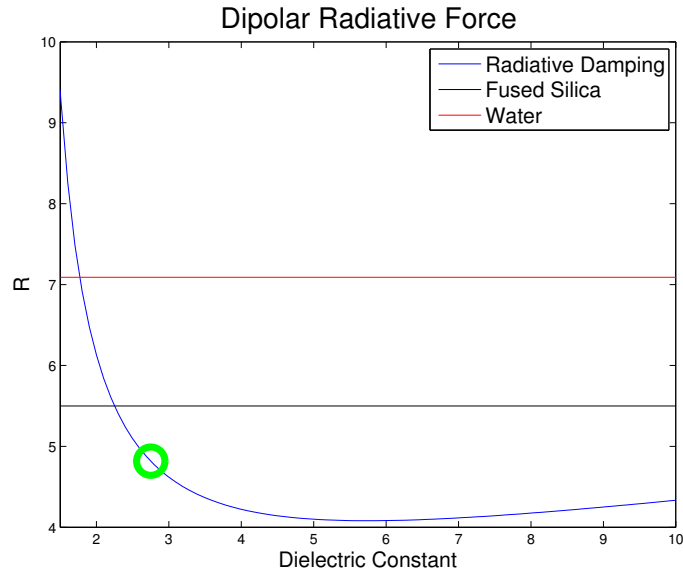


Figure 5.5: The blue curve represents the radiative force for a dipole, which is expressed in equation 2.30. The horizontal lines are the forces for fused silica and water at their respective dielectric constant. The green circle is the value of the dipolar radiative force. If the dipolar radiative dampening would be the reason for the dampened electron oscillations, the green ring should be above the two horizontal lines.

A possible explanation of the dampening could also be electron scattering at the border between partially reduced graphene oxide flakes and the surface of the gold nanoparticles, but the free electron path, in gold at relevant energies, is small compared to the particle

sizes [19].

Another explanation could be the graphene flakes, which are good conductors, and it is plausible that the flakes were channeling away electrons and thus damping the plasmon oscillations.

### 5.3 Angular Measurements

The absorption spectrum and the peak shifts for different samples was interesting, but the main advantage of the spherical vacuum chamber was the angular measurements.

#### 5.3.1 Angular Scattering Intensities

The angular scattering intensities revealed the intensity distribution for the graphene oxide samples, with or without gold nanoparticles.

Figure 5.6 shows the raw polar values for three different samples: fused silica substrate, graphene oxide and gold nanoparticles embedded in graphene oxide. The intensities are counts registered by the spectrometer. The values were corrected for different *UV*-lamp intensities between the measurements. The size differences of the samples was also corrected. Increasing sample area was assumed to linearly increase the scattered light. The graphene oxide concentration was not equal for the samples containing graphene oxide. The concentration difference was also corrected.

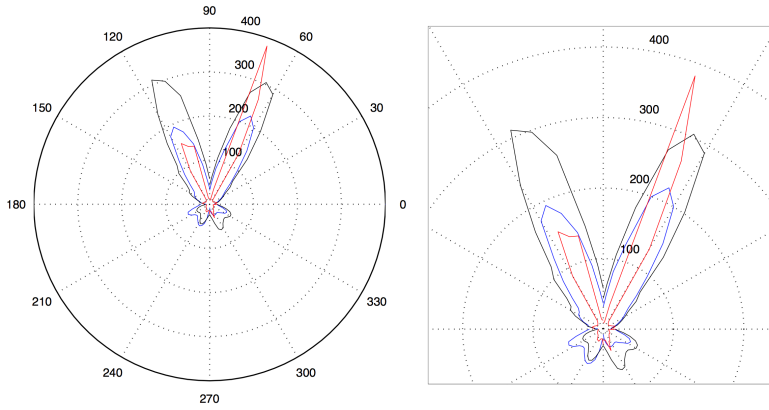


Figure 5.6: The figure shows the polar counts for the different samples at 540 nm. The figure at the right is a enlarged figure of the left figure. The red curve represents the pure gold nanoparticle sample, the black curve represents the graphene oxide sample and the blue curve represents the mixed graphene oxide and gold nanoparticle sample.

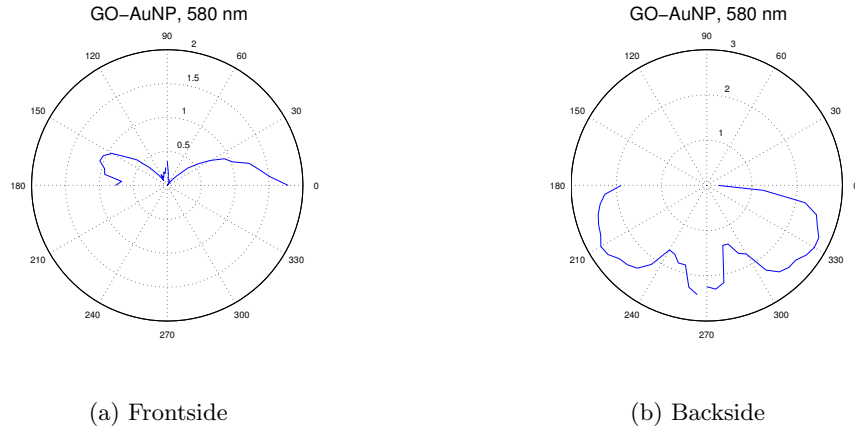


Figure 5.8: Angular scattering intensities at 580 nm for GO-AuNP sample. The intensities are the difference between the light source and the GO-AuNP sample.

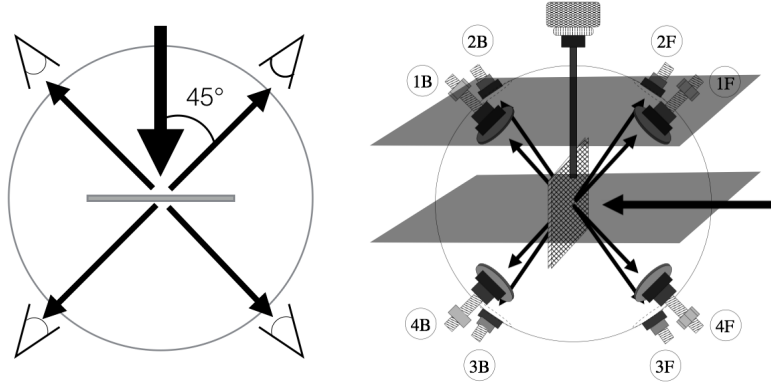


Figure 5.7: The measurement points and the incident light are not in the same plane. The angles in the polar graphs originate from the Z-manipulator. The angles in the polar graphs show a two-dimensional projection of the three-dimensional system.

The red curve in figure 5.6 was a test measurement of a pure fused silica substrate, and had a narrow shape. The black and the blue curves are the angular raw data of the samples with graphene oxide and graphene oxide mixed with gold nanoparticles. These have a broader shape, which probably was due to surface roughness. The fused silica substrate had a flatter surface and this led to a narrower shape in figure 5.6. Another observation was the reflection angle. From the geometry of the setup it was expected to have reflection at  $30^\circ$  from the incident light. The angular values in the angular figures is the angles which the manipulator is rotated. If the incident light and observation points were located in the same plane, the reflection angles in figure 5.6 would be  $30^\circ$ . But the incident light was not in the same plane as the observation point. The angle of reflection was most certainly at  $30^\circ$ , but is different in figure 5.6 because the angular values for the manipulator is a two dimensional projection from the top of the two planes.

The raw angular intensities in figure 5.6 does not tell us about the scattering from the particles. After normalization, the difference of lamp spectrum and the measured values at different angles is presented as a polar plot in figures 5.8 and 5.9. The overall shape of GO

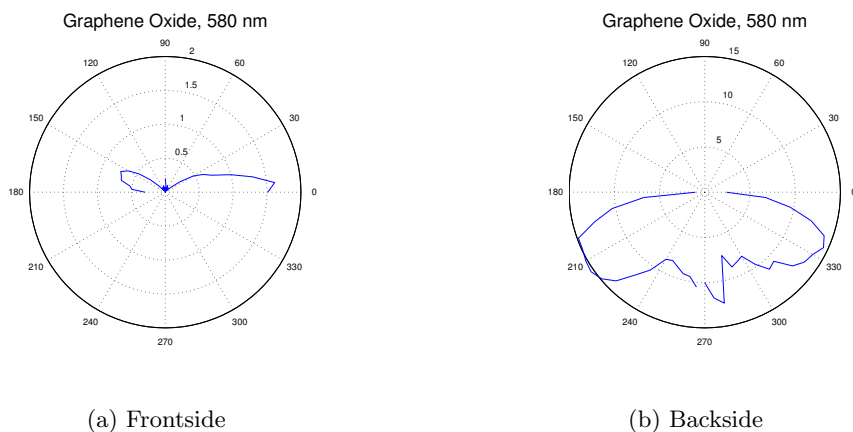


Figure 5.9: Angular scattering intensities at 580 nm for GO sample. The intensities are the difference between the light source and the graphene oxide sample.

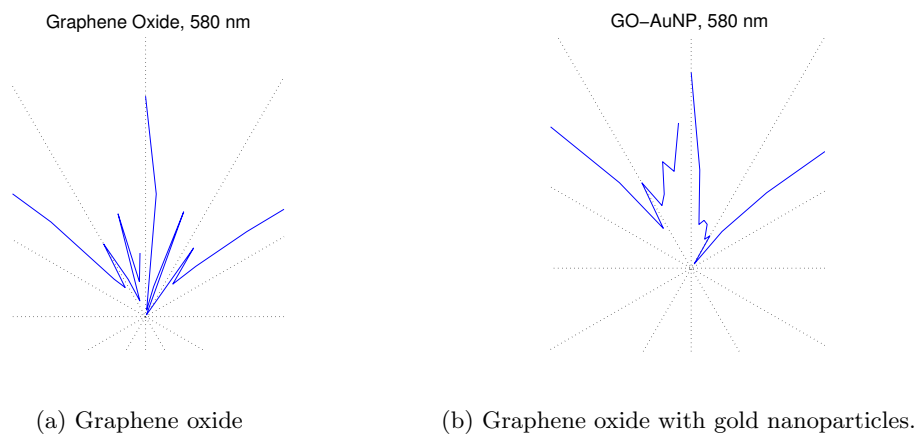


Figure 5.10: The two images are enlarged polar plots of the GO and GO-AuNP frontscattered intensities, figure 5.8a and 5.9a

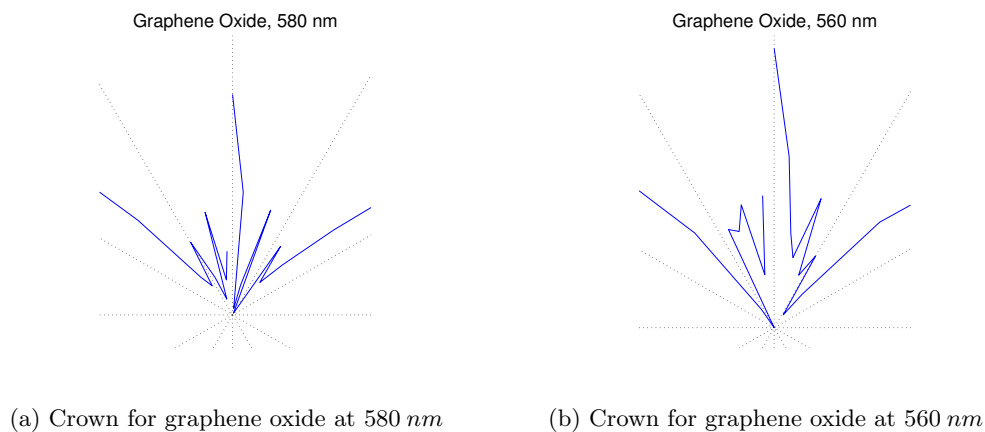


Figure 5.11: The two figures show the crowns for the graphene oxide sample at two wavelengths. The angles change depending on the wavelength.

and *GO-AuNP* was similar. The arms of the frontside scattered light of the graphene oxide sample had a slightly broader shape compared to the *GO-AuNP* sample. The interesting part of the frontside polar intensity plot was the crown shape of graphene oxide at angles close to the normal of the sample surface. This can be observed figure ???. The crown was not as prominent for the *GO-AuNP* sample.

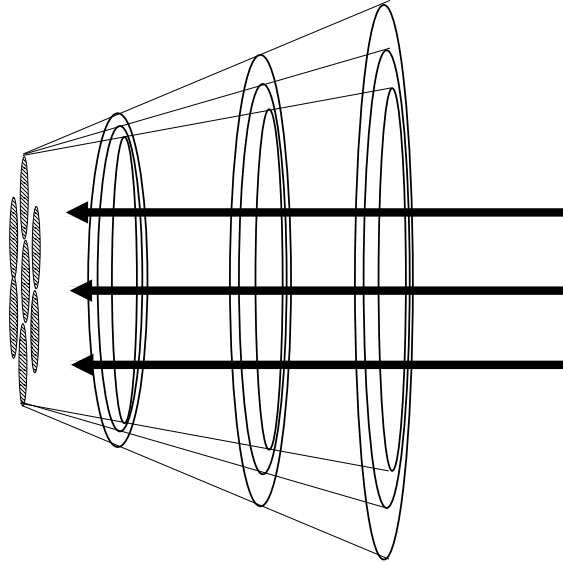


Figure 5.12: Diffraction is one possible explanation of the crowns. The partially reduced graphene oxide contains graphene flakes, which reflects light. Reflecting flakes could create a circular diffraction pattern.

The reason for the crown shape for graphene oxide could be diffraction. If Bragg's law is used with assumptions that the last arm was the fifth order at a angle of  $32.5^\circ$ , I come to the conclusion that the flake size was  $5.4 \mu\text{m}$ .  $5.4 \mu\text{m}$  was reasonable, since the specified size from the manufacturer was  $0.5 - 5 \mu\text{m}$ . If diffraction was the cause of the crown shape, the arms of the crown should change angles when the wavelength changed. The comparison of the crowns for  $580$  and  $560 \text{ nm}$  can be viewed in figure 5.11. The last arm of the  $560 \text{ nm}$  crown, at both sides, was less angled compared to the last arm for  $580 \text{ nm}$ . The decrease in angle was expected from Bragg's law. The angular resolution was  $5^\circ$ , which was low for a good analysis of the crowns. I believe there were more arms in the crowns, but I only saw two arms at each side, possibly due to low angular resolution. When using Bragg's law, assuming second or third order for the arms at  $\sim 30^\circ$ , does not lead to accurate values for the arms at  $\sim 15 - 20^\circ$ . According to Bragg's law, we should have a arm at  $\sim 10^\circ$ . At a close inspection at the crowns I saw a corner at  $\sim 10^\circ$ , but the resolution was probably not great enough to resolve these first order arms.

For diffraction to occur, multi layered partially reduced graphene oxide must be reflective enough. It is reported in other studies that the contrast of multi layered graphene in contrast measurements show increased contrast for increasing layers [21]. Furthermore, the extinction and absorption of light decreases and scattering increases as the number of graphene layers increases [16].

The structure of the surface could also affect the crown shape. The graphene oxide was

suspended in a aqueous solution, and basic solutions lead to uniform films [13]. The gold nanoparticles were suspended in a acidic solution. Acidic solutions leads to graphene oxide flakes forming clusters [13]. It is possible that the acidic solution has changed the surface structure and therefore resulted in the disappearance of the crown.

To draw further conclusions, different types, thicknesses and solution  $pH$  of graphene must be studied.

The backside polar intensities showed differences between graphene oxide with and without gold nanoparticles. The *GO* sample had a flatter angular intensity shape, the arms for the *GO-AuNP* was more prominent. The amplitudes for the backside intensities were larger compared to the frontside for both samples. The reason for the higher backscattered intensity for graphene oxide is unknown, but could be due to higher *GO* concentration compared to the *GO-AuNP* sample.

### 5.3.2 Angular Absorption Spectrum

The results above revealed the angular distribution of intensity at specific wavelengths, but not peak positions at different directions of measurement. Therefore, the natural following step in the study of the samples was performing angular resolved scattering peaks.

Figure 5.14 and 5.15 represents the spectral difference between source and signal for graphene oxide with gold nanoparticles. The data represents the total scattering spectrum, including the fused silica glass substrate. The glass substrate had a absorption spectrum, which was not subtracted in the figures 5.14 and 5.15. The graphs show the comparison between different angles. The angles in figures 5.14, 5.15, 5.16, 5.17, 5.19 and 5.18, was the angles between the normal of the substrate and the relevant measurement point.

The data was normalized at the wavelength  $\lambda = 431 \text{ nm}$ . The *UV*-lamp had a high intensity around  $\lambda \sim 400 - 500 \text{ nm}$ . Differences between measurements are the greatest in this region. If the spectrum was normalized far beyond  $\lambda \sim 400 - 500 \text{ nm}$ , faulty spectrum with absorption peaks at shorter wavelengths were obtained. The faulty peaks had the spectral shape of the *UV*-lamp, because the largest differences, between samples and measurements, were at the wavelengths where the *UV*-lamp had its maximum intensity. The odd value of  $431 \text{ nm}$  was simply chosen because the wavelength data from the data sheet, coming from the spectrometer software did not start at a even wavelength. It would be catastrophic if the peaks would change depending on normalizing wavelength. The data was tested with different normalizing wavelengths and the peak positions were consistent. Figure 4.7 shows the principle of the measurements, and for frontside measurements points  $1F$ ,  $2F$ ,  $3F$  and  $4F$  were used. For the backside measurements points  $1B$ ,  $2B$ ,  $3B$  and  $4B$  were used. In general, I observed no peak shifts during sample rotation, but the amplitudes of the peaks changed.

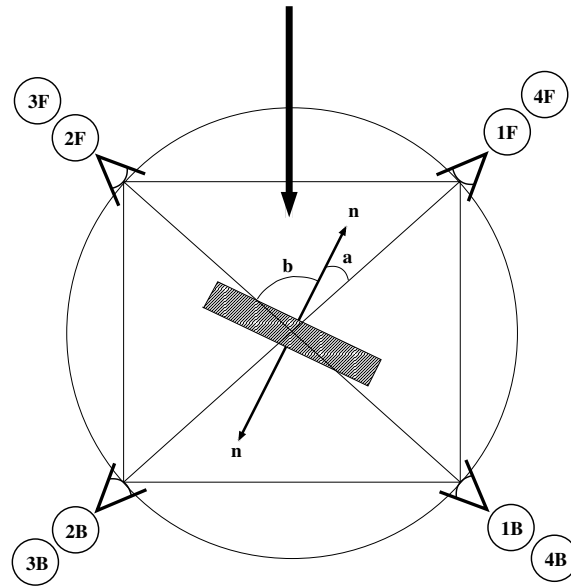
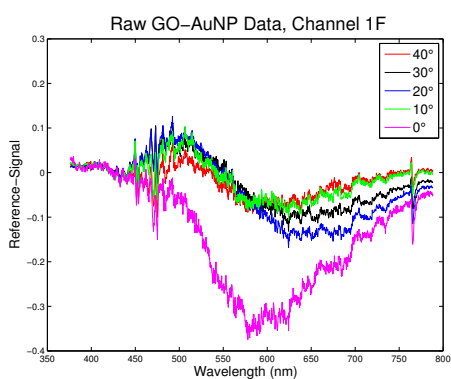
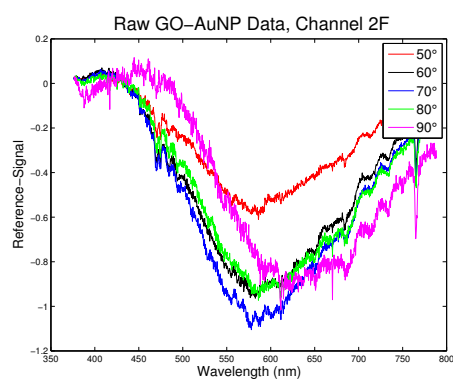


Figure 5.13: The figure is a two dimensional projection of the spherical chamber, which shows the angles which are used to describe the angular scattering spectrum. Angle  $a$  is used in the following graphs for channel 4F, 4F, 2B and 3B. Angle  $b$  is used for describing the angular data for the rest of the channels.

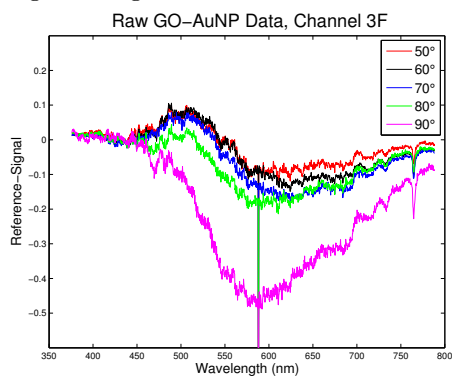
The results of many backside measurements, with the normal of the sample parallel to the incident light beam, were close to the characterized values. But several measurements on the frontside showed large variations between measurements. A additional test was conducted in order to test this. The light beam was directed at different parts of the sample and compared, illustrated in figure 5.20. Figure 5.21 shows examples of different measurements at different channels and direction of the incident light. I saw the spectrum varying dramatically. This could be explained by iridescence and structural coloring. Iridescence is a effect which is observed for thin films with thickness variations. Structural coloring could have occurred if the graphene oxide flakes formed a microstructure on the substrate.



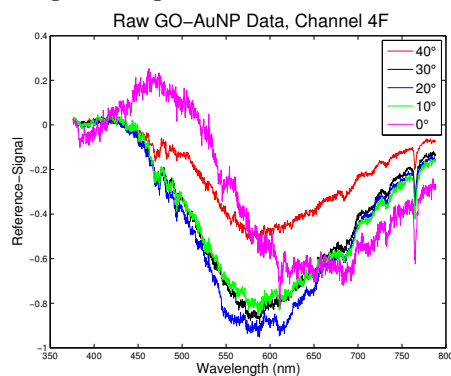
(a) Channel 1F. The angles correspond to angle a in figure 5.13



(b) Channel 2F. The angles correspond to angle b in figure 5.13

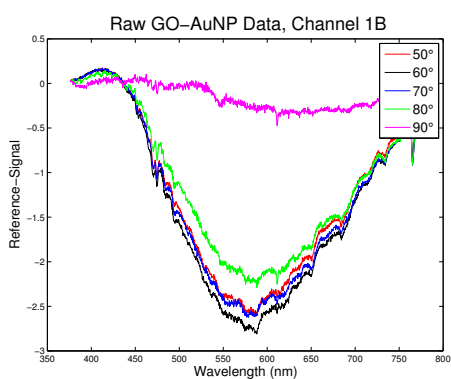


(c) Channel 3F. The angles correspond to angle a in figure 5.13

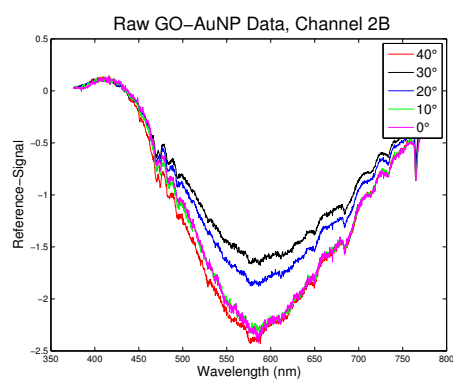


(d) Channel 4F. The angles correspond to angle b in figure 5.13

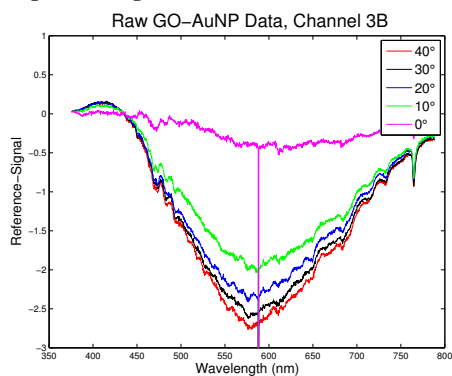
Figure 5.14: Frontside raw data of Au nanoparticles in a graphene oxide covered substrate.



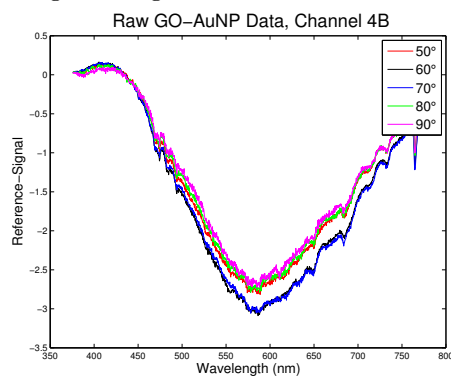
(a) Channel 1B. The angles correspond to angle b in figure 5.13



(b) Channel 2B. The angles correspond to angle a in figure 5.13

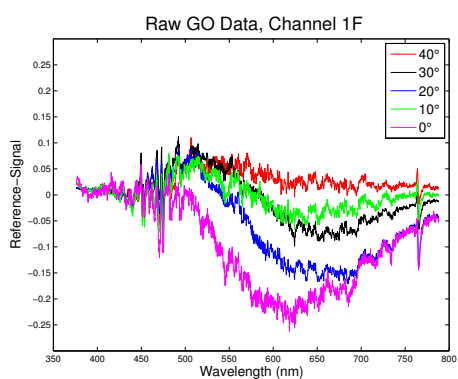


(c) Channel 3B. The angles correspond to angle a in figure 5.13

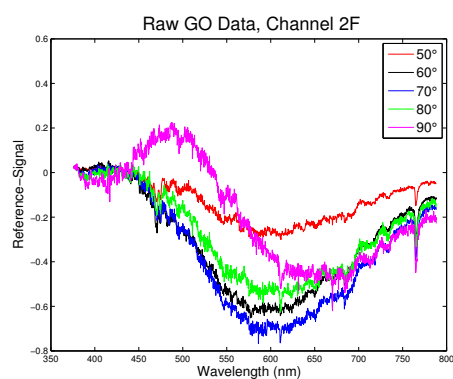


(d) Channel 4B. The angles correspond to angle b in figure 5.13

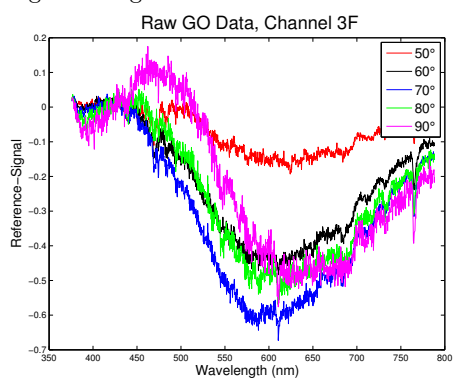
Figure 5.15: Backside raw data of Au nanoparticles in a graphene oxide covered substrate.



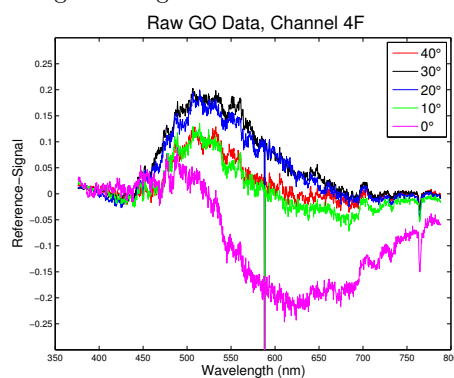
(a) Channel 1F. The angles correspond to angle a in figure 5.13



(b) Channel 2F. The angles correspond to angle b in figure 5.13

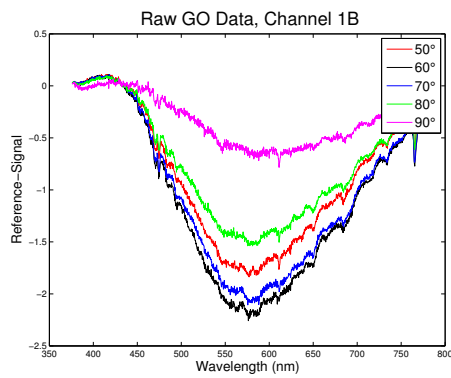


(c) Channel 3F. The angles correspond to angle b in figure 5.13

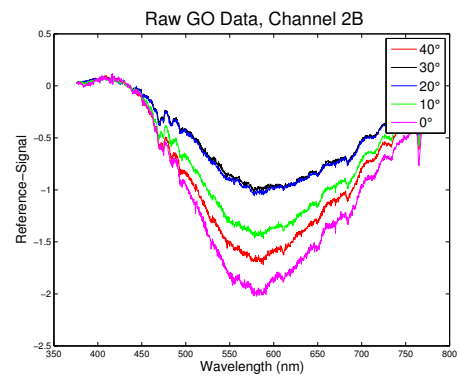


(d) Channel 4F. The angles correspond to angle a in figure 5.13

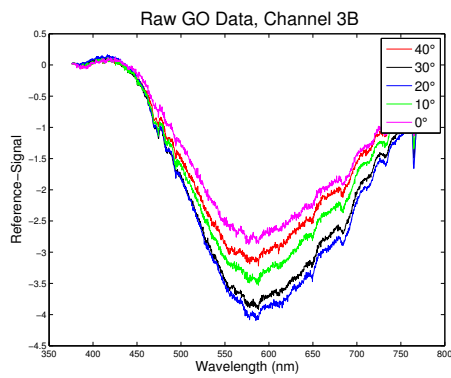
Figure 5.16: Frontside raw data of graphene oxide substrate.



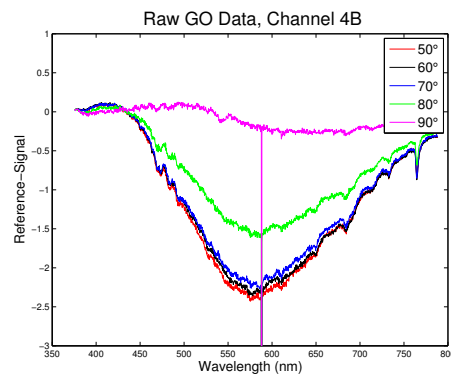
(a) Channel 1B. The angles correspond to angle b in figure 5.13



(b) Channel 2B. The angles correspond to angle a in figure 5.13

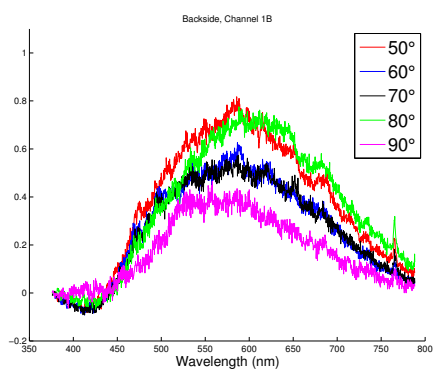


(c) Channel 3B. The angles correspond to angle a in figure 5.13

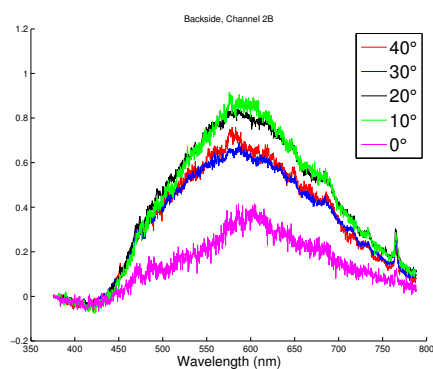


(d) Channel 4B. The angles correspond to angle b in figure 5.13

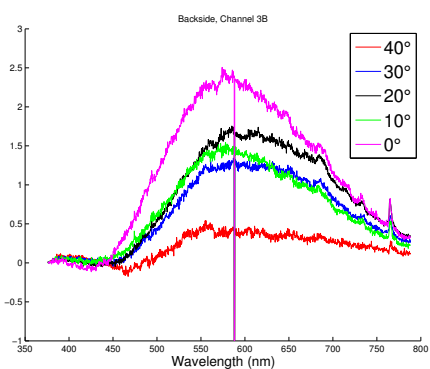
Figure 5.17: Backside raw data of graphene oxide substrate.



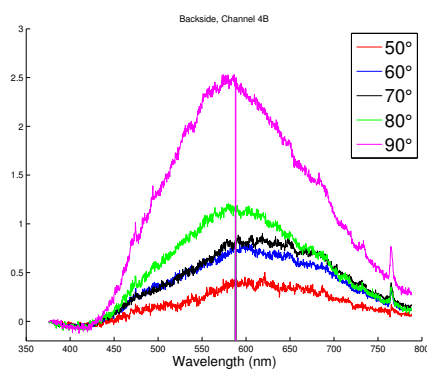
(a) Channel 1B. The angles correspond to angle b in figure 5.13



(b) Channel 2B. The angles correspond to angle a in figure 5.13

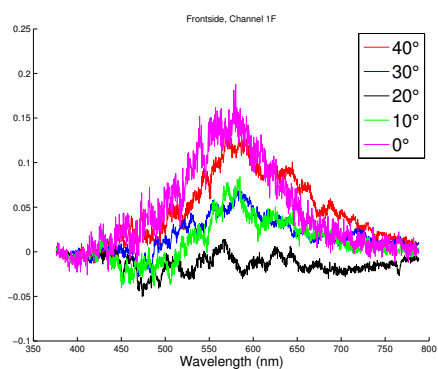


(c) Channel 3B. The angles correspond to angle a in figure 5.13

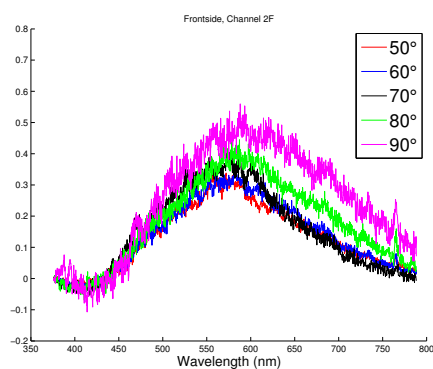


(d) Channel 4B. The angles correspond to angle b in figure 5.13

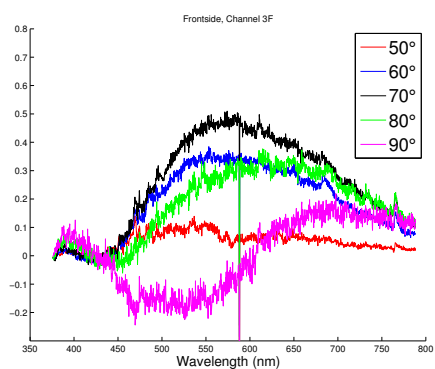
Figure 5.18: The figures represent the difference between GO sample and GO-AuNP sample. These figures show backside data



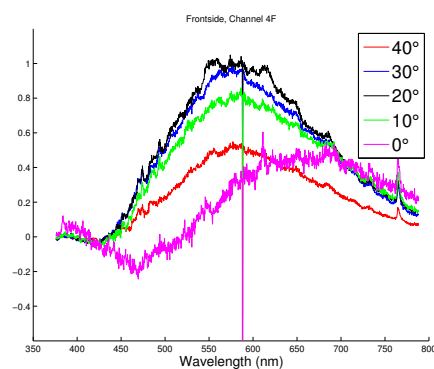
(a) Channel 1F. The angles correspond to angle a in figure 5.13



(b) Channel 2F. The angles correspond to angle b in figure 5.13



(c) Channel 3F. The angles correspond to angle b in figure 5.13



(d) Channel 4F. The angles correspond to angle a in figure 5.13

Figure 5.19: The figures represent the difference between GO sample and GO-AuNP sample. These figures show frontside data

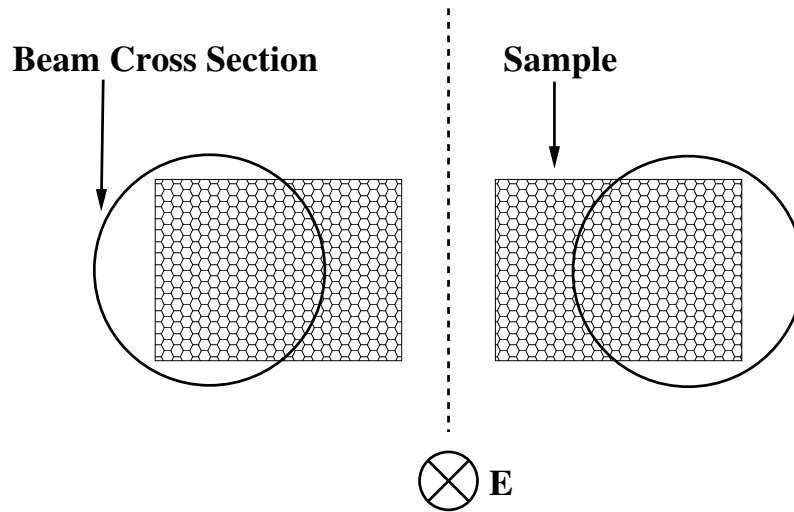


Figure 5.20: Iridescence was suspected to cause the large differences between independent measurements. Tests were performed to test if the direction of the light beam could affect the data.

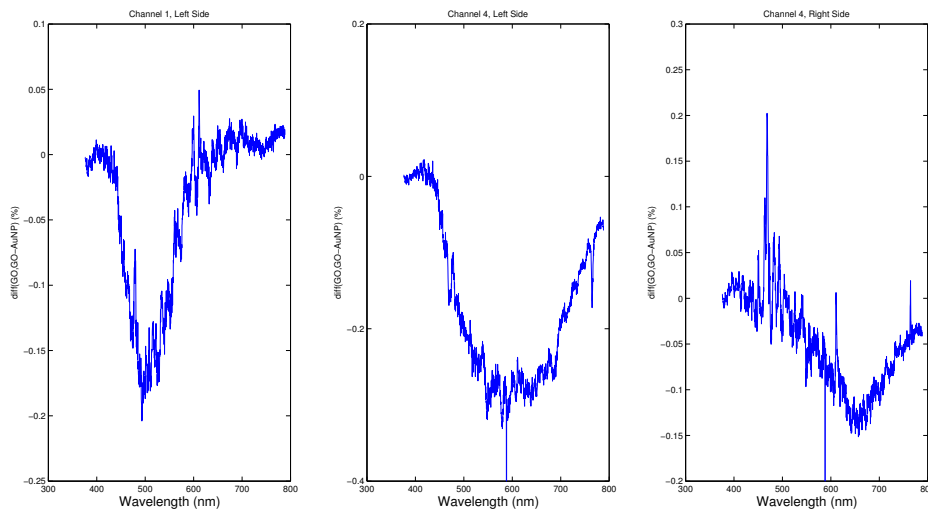


Figure 5.21: Figures show peaks for different channels and for different directions of the incident light beam. The differences were large, up to 150 nm in difference. The peak width is also different for different measurements.

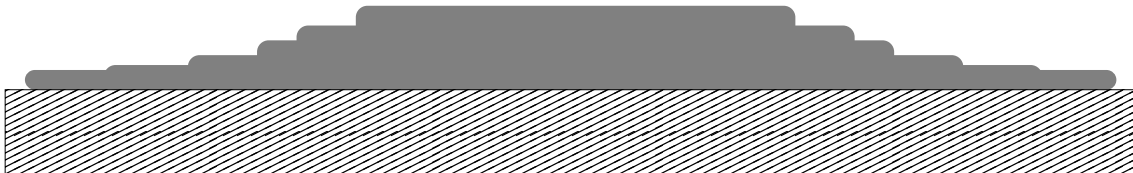
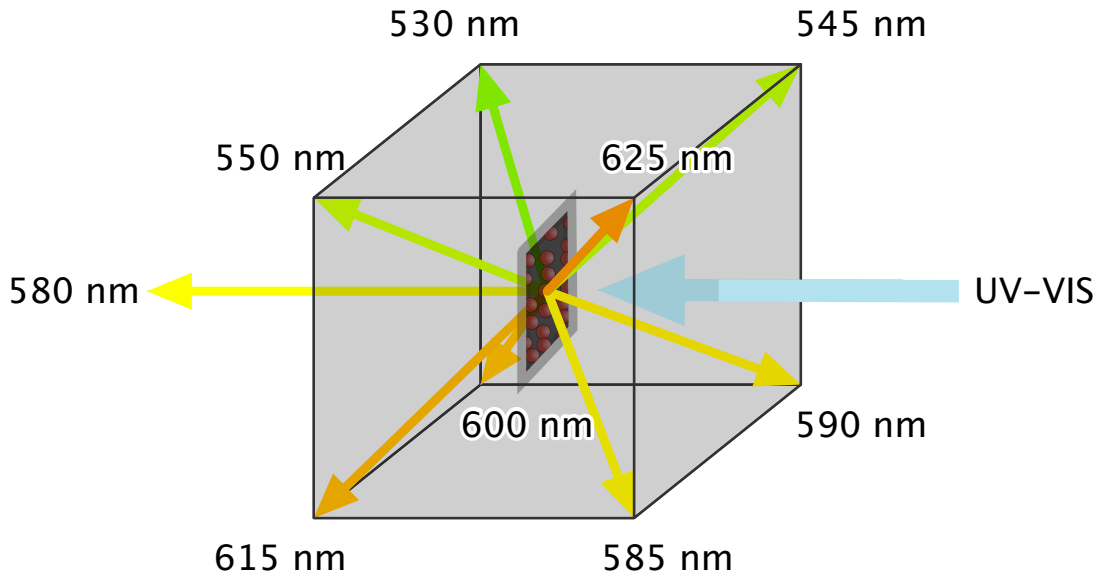


Figure 5.22: Due to the sample preparation method, the samples had thickness variations across the surface. Color shifts was most visible at the ends of the GO-AuNP sample. The ends were later removed and measurements performed in the middle of the sample

At a closer inspection of the samples, iridescence of the samples was visible to the naked eye. The iridescence originated from the manufacturing technique. Example of the thickness variation is illustrated in figure 5.22. Droplets, containing *GO* and/or gold nanoparticles, dried from the outside in, making the droplet shrink to the middle part of the substrate during drying. The samples were fairly homogeneous in thickness at the middle of the samples. After comparing *GO* and *GO-AuNP* samples, the *GO-AuNP* was notably more homogeneous in thickness compared to pure *GO* sample. The contact angle of the droplets affect the homogeneity [20], which was not studied during sample preparation.

More precise measurement was conducted, by decreasing the cross section of the light beam and by only measuring at the middle of the samples. The results can be seen in figure 5.23. The large value at channel *1F* was not explainable. The differences between neighboring channels at the same plane were  $5 - 20 \text{ nm}$ . Peak wavelengths at channels *2B* and *3B* were smaller compared to the opposing channels *1B* and *4B*. It is likely that different components in the scattered light was causing this difference. Peak wavelength channel *4F* was also smaller compared to channel *3F*. This difference is logical. The diagonal similarity between *2B* and *4F* should occur if a additional component is causing the differences in peak wavelength.



*Figure 5.23: The figure shows the peaks of the scattered light at different directions. The colors of the arrows accurately represents the wavelengths. The ends of the sample is removed in the final measurements leading to the results in this figure, in order to eliminate iridescence. I observed differences between the channels. The upper parts scattered light at slightly shorter wavelengths and the bottom part scattered towards longer wavelengths. There were also differences side to side. The closest channels at the back showed slightly longer wavelengths compared to the far back channels. The opposite was true for the front channels. A possible explanation is illustrated in the following figure 5.24. The cause of the high value at channel *1F* is unclear.*

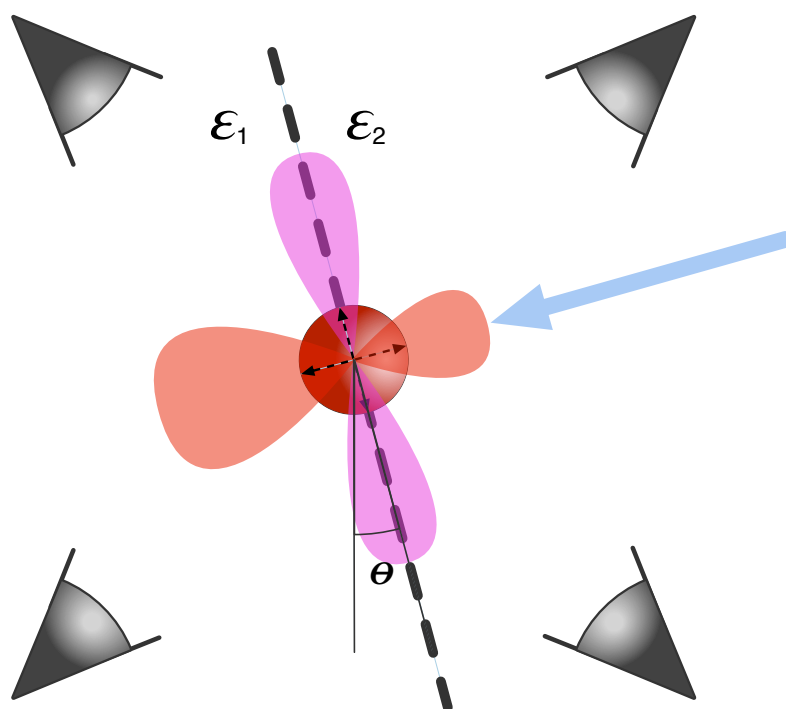


Figure 5.24: The reason for the shifts between the channels in figure 5.23 could be due to multiple components. The graphene oxide flakes could cause differences in the dielectric constant between the part where the particles were in contact with GO, and air. If one component affects one measurement channel, the diagonally opposite channel would also be affected by the same component. But only if the light source is directed at the sample with a angle. The light source and the spherical vacuum chamber were not perfectly alligned during the experiments. The differences between the channels is not expected for a perfectly alligned light source, vacuum chamber and sample. The drawing is a top view of the spherical chamber.



## Chapter 6

# Conclusions and Outlook

With the experiments I was able to measure shifts in the plasmon resonance frequencies for different environments. Besides the shift, the shape of the peaks also gave information about the surroundings. Graphene oxide apparently dampens the plasmon oscillation. The radiative model for a dipole does not answer if the radiative damping is the reason. Instead an analysis of the quadrupole mode is needed. Another possible explanation for the oscillation damping could be electrons escaping the particles through the partially reduced graphene oxide flakes. The angular resolved measurements led to many interesting results. The raw angular data revealed the reflection angles and the surface roughness, the latter leading to broader shaped arms in the raw angular intensity plots. The more interesting angular scattering intensities was also studied.

The scattering intensities at angles around the surface normal, at  $580\text{ nm}$ , revealed a crown for the frontside scattered light. One theory is that diffraction is causing the crown shape for the partially reduced graphene oxide flakes. According to Bragg's law the flakes should have a diameter of  $\sim 5\mu\text{m}$ , which is close to the specified value of  $0.5 - 5\mu\text{m}$ . The crown was plotted for  $560\text{ nm}$ , which led to decrease in the angles of the crown arms. The change in angles is supported by Bragg's law. The crown arms were smeared out for the *GO-AuNP* sample. The thickness of the graphene oxide layer affects the reflectivity and the solution *pH* determines the surface structure. SEM images and further studies are needed to draw further conclusions.

Differences for back scattered light, between the different samples, were observed. The back scattered intensities were much higher with gold nanoparticles in the sample. Higher intensities for back scattered light is expected from Mie scattering. The *GO-AuNP* sample also had a flatter back scattered intensity shape compared to sample with only graphene oxide.

Besides studying peak shifts and angular intensities, peaks for the scattered light at different angles were compared. Many independent measurements showed large differences in peak position between each other. The cause for these unstable data was probably due to the iridescence phenomena, caused by thickness variations across the sample.

To test the iridescence phenomena, the light beam was directed at different parts of the sample. Differences in incident angle and beam position caused huge differences in scat-

tering spectrum. The differences were as great as 150 *nm*.

After inspection of the sample, the iridescence effect was visible to the naked eye. The iridescence was occurring mostly at the edges of the sample.

The edges of the samples were removed, and a test where the light beam was directed at the middle of the sample was conducted. The peak position between the different channels were more comparable. 5 – 20 *nm* differences were observed for opposing channels, which possibly indicate several components of the scattered light.

In general, all measurement were probably affected by iridescence. Future improvements for similar experiments would be in the sample preparation process. With a more precise manufacturing technique, even samples could be manufactured and better results obtained. The topic is interesting and many previously unknown effects were revealed during the experiments, but I did not have time to study these effects in detail. Future measurements could also include different sized nanoparticles, so the effects of the different modes can be studied.

# Bibliography

- [1] E. Ringe, B. Sharma, A-I Henry, L.D. Marks, R.P. Van Duyne, Single nanoparticle plasmonics, *Phys. Chem. Chem. Phys.*, vol. 15, nr. 12, pp. 4110-4129, feb. 2013. doi: 10.1039/C3CP44574G
- [2] J. Olson, S. Dominguez-Medina, A. Hoggard, L-Y. Wang, W-S. Chang, S. Link, Optical characterization of single plasmonic nanoparticles, *Chem. Soc. Rev.*, vol. 44, nr. 1, pp. 40-57, jun. 2014. doi: 10.1039/C4CS00131A
- [3] R.B. Miles, W.R. Lempert, J.N. Forkey, Laser Rayleigh scattering, *Meas. Sci. Technol.*, vol. 12, feb. 2001.
- [4] K.L. Kelly, E. Coronado, L.L. Zhao, G.C. Schatz, The Optical Properties of Metal Nanoparticles: The Influence of Size, Shape, and Dielectric Environment, *J. Phys. Chem. B*, vol. 107, nr. 3, pp. 668-677, dec. 2002. doi:10.1021/jp026731y
- [5] N.I. Grigorochuk, Radiative damping of surface plasmon resonance in spheroidal metallic nanoparticle embedded in a dielectric medium, *J. Opt. Soc. Am. B*, vol. 29, nr. 12, dec. 2012. doi: 10.1364/JOSAB.29.003404
- [6] K-N, Liou, A Complementary Theory of Light Scattering by Homogeneous Spheres, *Applied Mathematics and Computation archive*, vol. 3, nr. 4, pp. 331-358, jan. 1977. doi:10.1016/0096-3003(77)90018-2
- [7] U. Kreibig, M. Vollmer, *Optical Properties of Metal Clusters*. Berlin: Springer-Verlag Berlin, 1995.
- [8] G. Mie, Contributions on the Optics of Turbid Media, Particularly Colloidal Metal Solutions, *Annalen der Physik, Series IV*, vol. 25, nr. 3, pp. 377-445, 1908.
- [9] M. Bosman, E. Ye, S.F. Tan, C.A. Nijhuis, J.K.W. Yang, R. Marty, A. Mlayah, A. Arbouet, C. Girard, M-Y. Han, Surface Plasmon Damping Quantified with an Electron Nanoprobe, *Scientific Reports*, vol. 3, nr. 1312, feb. 2013. doi: 10.1038/srep01312
- [10] M. Pelton, G.W. Bryant, *Introduction to Metal-Nanoparticle Plasmonics*. Wiley, 2013.
- [11] H. Weinrib, A. Meiri, H. Duadi, D. Fixler, Uniformly Immobilizing Gold Nanorods on a Glass Substrate, *Journal of Atomic, Molecular, and Optical Physics*, vol. 2012, apr. 2012. doi:10.1155/2012/683830
- [12] G. Baffou, On the optical properties of gold and gold nanoparticles, *Phys. Rev. B*, vol. 6, nr. 4370, 1972.

- [13] G.J. Silverberg, P. Pearce, C.D. Vecitis, Controlling Self-Assembly of Reduced Graphene Oxide at the Air Water Interface: Quantitative Evidence for Long-Range Attractive and Many-Body Interactions, *ACS Appl. Mater. Interfaces*, vol. 7, nr. 6, pp. 3807–3815, jan. 2015. doi: 10.1021/am5087984
- [14] S. Kashyap, S. Mishra, S.K. Behera, Aqueous Colloidal Stability of Graphene Oxide and Chemically Converted Graphene, *Journal of Nanoparticles*, vol. 2014, nov. 2014. doi: <http://dx.doi.org/10.1155/2014/640281>
- [15] M.M. Miller, A.A. Lazarides, Sensitivity of Metal Nanoparticle Surface Plasmon Resonance to the Dielectric Environment, *J. Phys. Chem. B*, vol. 109, nr. 46, pp. 21556–21565, oct. 2005. doi: 10.1021/jp054227y
- [16] J. Wu, W. Shi, N. Chopra, Optical properties of gold/multilayer-graphene/carbon nanotube hybrid materials, *Carbon*, vol. 68, pp. 708–717, mar. 2014. doi: 10.1016/j.carbon.2013.11.052
- [17] R. Kitamura, L. Pilon, M. Jonasz, Optical constants of silica glass from extreme ultraviolet to far infrared at near room temperature, *Applied Optics*, vol. 46, nr. 33, nov. 2007. doi: 10.1364/AO.46.008118
- [18] S. Cheon, K.D. Kihm, H.G. Kim, G. Lim, J.S. Park, J.S. Lee, How to Reliably Determine the Complex Refractive Index (RI) of Graphene by Using Two Independent Measurement Constraints, *Scientific Reports*, vol. 4, sep. 2014. doi: 10.1038/srep06364
- [19] H. Kanter, Slow-Electron Mean Free Paths in Aluminum, Silver, and Gold, *Phys. Rev. B*, vol. 1, nr. 2, jan. 1970. doi: <http://dx.doi.org/10.1103/PhysRevB.1.522>
- [20] Y. Guo, C-A. Di, H. Liu, J. Zheng, L. Zhang, G. Yu, Y. Liu, General Route toward Patterning of Graphene Oxide by a Combination of Wettability Modulation and Spin-Coating, *ACS Nano*, vol. 4, nr. 10, sep. 2010. doi: 10.1021/nn101463j
- [21] Z.H. Ni, H.M. Wang, J. Kasim, H.M. Fan, T. Yu, Y.H. Wu, Y.P. Feng, Z.X. Shen, Graphene Thickness Determination Using Reflection and Contrast Spectroscopy, *Nano Lett.*, vol. 7, nr. 9, pp. 2758–2763, jul. 2007. doi: 10.1021/nl071254m
- [22] Y.H. Fu, A.I. Kuznetsov, A.E. Miroshnichenko, Y.F. Yu, B. Luk'yanchuk, Directional visible light scattering by silicon nanoparticles, *Nature Communications*, vol. 4, feb. 2013. doi: 10.1038/ncomms2538